POLYMER NANOCOMPOSITE PROTECTIVE COATINGS DEPOSITED USING LAYER-BY-LAYER ASSEMBLY

A Dissertation

by

SHUANG QIN

Submitted to the Office of Graduate and Professional Studies of
Texas A&M University
in partial fulfillment of the requirements for the degree of

DOCTOR OF PHILOSOPHY

Chair of Committee,	Jaime Grunlan
Committee Members,	Homero Castaneda
	Yossef Elabd
	Micah Green
Head of Department,	Ibrahim Karaman

May 2019

Major Subject: Materials Science and Engineering

ABSTRACT

Protective coatings with the ability to shield the materials underneath are crucial to packaging, flame retardancy, and corrosion prevention. Amongst all the desired properties, barrier performance is critical for protective coatings. Packaging requires gas barrier and corrosion protection becomes more efficient with a good barrier against corrosive species. Polymer-clay composites have shown great potential as protective coatings due to their cost efficiency, ease of production, and good mechanical properties, and more importantly, good barrier due to the torturous pathway created by impermeable clay. Despite these benefits, further improvements are limited because of clay aggregation and misalignment within polymer matrices. Layer-by-layer assembly (LbL) has proven to be a cost-effective technique that enables high clay loading (> 60 wt%) in thin film coatings. This dissertation is focused on utilizing LbL assembly to achieve a high level of clay alignment and loading in unconventional polymer matrices for varying applications, along with the development of new functionalities.

Hydrogen-bonded all-polymer systems are highly stretchable but they suffer from low barrier. In an effort to improve barrier performance while maintaining stretchability, clay platelets were introduced to a hydrogen-bonded system by the alternate deposition of poly(ethylene oxide) (PEO) and polyacrylic acid (PAA) mixed with montmorillonite (MMT) clay. This system, with aligned clay, provides the best stretchable oxygen barrier to-date.

In addition to MMT, vermiculite (VMT) clay, with larger aspect ratio, is known to impart better barrier when incorporated into LbL systems. In an effort to improve the barrier and flame resistance of biodegradable polymers such as cellulose, VMT clay is paired with modified cellulose nanofibrils (CNF) (that have positively charged surfaces) using LbL assembly. The resulting nanobrick wall thin film structure imparts great improvement in oxygen barrier, flame resistance, and modulus.

LbL-assembled polymer-clay films also demonstrate good corrosion protection. A 30-bilayer waterborne polyurethane and VMT coating, with a thickness of 300 nm, provides 100X improvement in impedance and remains effective for at least five days. This is a result of relatively high hydrophobicity and the nanobrick wall structure, making it a potential environmentally-friendly replacement for toxic chromate conversion coatings (CCCs).

DEDICATION

I would like to dedicate this dissertation for my dearest parents, Huiling and Qun, thank you for supporting every choice I made all these years. I also want to dedicate this work to my fiancé Yixuan, who has given me constant love and support. I am truly thankful for having you in my life. This is also for Mr. Huang, my longtime best friend and favorite bird. You colored my childhood and may you rest in peace.

ACKNOWLEDGEMENTS

I would like to express my deepest appreciation to my adviser and committee chair, Dr. Jaime Grunlan, who provided guidance and endless support during the past few years. I am grateful that when I wanted to explore new research areas, he gave me the freedom and contributed valuable feedback and the resources I needed. All these experiences prepared me for my future career as a research scientist. I would also like to thank my committee members, Dr. Micah Green, Dr. Yossef Elabd, and Dr. Homero Castaneda, for their help throughout the course of my research.

I also want to thank my colleagues in Polymer Nanocomposite Laboratory for their help in both my research and life, including Dr. Ryan Smith, Dr. Yixuan Song, Dr. Kevin Holder, Dr. Merid Haile, Dr. Chungyeon Cho, Dr. Mario Culebras, Simone Lazar, Thomas Kolibaba, Carolyn Long, Xiaodong Liu, Dan Stevens and Hsu-Cheng Chiang. I also want to thank my undergraduate assistants, Kyle Falke, Joseph Gerringer, and Bailey Eberle, I could not finish my work within four years without their contributions. I also had great pleasure of working with many talented scientists in Sandia National Laboratories including Dr. Eric Schindelholz, Dr. Erik Spoerke, and Dr. Stephen Percival. I would also like to thank Dr. Castaneda and Yenny Cubides for their contributions in my corrosion project, Dr. Yordanos Bisrat and Dr. Wilson Serem for their help with SEM and AFM.

Thanks also go to my friends at Texas A&M University, especially Baiyu, Ramatou, Yenny, Lian, Sisi, and Simone for their company and support. I also want to thank my best friend Lanbing for her friendship, may you and Ting live happily ever after.

CONTRIBUTORS AND FUNDING SOURCES

Contributors:

This work was supervised by Professor Jaime Grunlan and the rest of the dissertation committee including Prof. Homero Castaneda and Prof. Micah Green of the Department of Materials Science and Engineering and Prof. Yossef Elabd of the Department of Chemical Engineering.

The cellulose nanofibrils in Chapter 4 were provided by Dr. Maryam Ghanadpour and Prof. Lars Wagberg, and the impedance data in Chapter 5 was analyzed by Ms. Yenny Cubides. Some of the experiments in Chapter 3-5 were conducted by Mr. Michael Floto, Mr. Joseph Gerringer, and Mr. Kyle Falke.

All other work in this thesis was completed by the student independently.

Funding Sources:

This work was made possible by National Science Foundation (CBET 1403686) and the Laboratory Directed Research and Development program at Sandia National Laboratories. Sandia National Laboratories is a multi-mission laboratory managed and operated by National Technology and Engineering Solutions of Sandia, LLC., a wholly owned subsidiary of Honeywell International, Inc., for the U.S. Department of Energy's National Nuclear Security Administration under contract DENA0003525.

NOMENCLATURE

PVD	Physical Vapor Deposition
CVD	Chemical Vapor Deposition
LbL	Layer-by-layer Assembly
PEO	Poly(ethylene oxide)
PEI	Poly(acrylic acid)
PAA	Polyethyleneimine
MMT	Montmorillonite
VMT	Vermiculite
PU	Polyurethane
CNF	Cellulose Nanofibrils
PEM	Polyelectrolyte Multilayers
PET	Poly(ethylene terephthalate)
SiOx	Silicon Oxide
BL	Bilayer
QL	Quadlayer
WVTR	Water Vapor Transmission Rate
OTR	Oxygen Transmission Rate
QCM	Quartz Crystal Microbalance
AFM	Atomic Force Microscope
UV-vis	Ultraviolet–Visible

SEM	Scanning Electron Microscopy
TEM	Transmission Electron Microscopy

TABLE OF CONTENTS

Page

ABSTRACT ii

DEDICATION iv

ACKNOWLEDGEMENTS v

CONTRIBUTORS AND FUNDING SOURCES vi

NOMENCLATURE vii

TABLE OF CONTENTS ix

LIST OF FIGURES xi

LIST OF TABLES xiv

CHAPTER I INTRODUCTION 1

1.1 Background 1
1.2 Dissertation Outline 2

CHAPTER II LITERATURE REVIEW 6

2.1 Protective Coatings: Gas Barrier 6
2.1.1 Gas Transport Theories 7
2.1.2 Gas Barrier Materials 10
2.1.3 Layer-by-Layer (LbL) Assembly of Gas Barrier Nanocoatings 20
2.2 Corrosion Protection Coatings 21
2.2.1 Chromate Conversion Coatings 23
2.2.2 Alternatives for Chromate Conversion Coatings 24

CHAPTER III COMBINED HIGH STRETCHABILITY AND GAS BARRIER IN HYDROGEN-BONDED MULTILAYER NANOBRICK WALL THIN FILMS 28

3.1 Introduction 28
3.2 Experimental 29
3.3 Results and Discussion 31
3.4 Conclusions 38

CHAPTER IV SUPER GAS BARRIER AND FIRE RESISTANCE OF NANOPLATELET/NANOFIBRIL MULTILAYER THIN FILMS 40

4.1 Introduction..... 40
4.2 Experimental..... 41
4.3 Results and Discussion..... 44
4.3.1 Thin Film Structure 44
4.3.2 Oxygen Barrier of Nanocoatings on Polyester..... 46
4.3.3 Flame Resistance Imparted to Polyurethane Foam 48
4.3.4 Mechanical Properties of Thin Films 51
4.4 Conclusions..... 52

CHAPTER V ULTRATHIN TRANSPARENT NANOBRICK WALL ANTICORROSION COATINGS 53

5.1 Introduction..... 53
5.2 Experimental..... 54
5.3 Results and discussion..... 56
5.3.1 Multilayer Film Morphology 56
5.3.2 Anticorrosion Performance..... 58
5.4 Conclusions..... 65

CHAPTER VI CONCLUSIONS AND FUTURE WORK..... 67

6.1 New and Improved Functionality Developments for Polyelectrolyte-Clay Assemblies..... 67
6.1.1 Combined High Stretchability and Gas Barrier in Hydrogen-Bonded Multilayer Nanobrick Wall Thin Films..... 67
6.1.2 Super Gas Barrier and Fire Resistance of Nanoplatelet/Nanofibril Multilayer Thin Films..... 68
6.1.3 Ultrathin Transparent Nanobrick Wall Anticorrosion Coatings 68
6.2 Future Directions..... 69
6.2.1. Improving Moisture Barrier of SiO_x with Polyelectrolyte Layers..... 69
6.2.2 Corrosion Protection Coatings with PEM Barrier Coating and Hydrophobic Surface..... 73

REFERENCES..... 75

LIST OF FIGURES

Page

Figure I-1. Schematic of layer-by-layer assembly (LbL) process. 2

Figure II-1. Schematic of the tortuous pathway in polymer/clay composites. Reprinted with permission from [reference 31].[31] 10

Figure II-2. Oxygen and water transmission rates of commonly used polymers in packaging. Reprinted from [reference 36].[36] 11

Figure II-3. The life cycle of biodegradable polymers. Reprinted with permission from [reference 39].[39] 12

Figure II-4. Schematic of typical process to obtain CNF. Reprinted with permission from [reference 48].[48] 13

Figure II-5. Digital photographs of pretreated CNF suspensions. Reprinted with permission from [reference 47].[47] 14

Figure II-6. (a) Schematic of the shadow effect in the PVD process.[36] (b) Oxygen transmission rate (OTR)-thickness relationship.[69] Adapted with permission from [reference 36 and 69]. 17

Figure II-7. A cross-sectional scanning electron microscope (SEM) image of four pairs (dyads) of Al_xO_y/polymer multilayer. Reprinted with permission from [reference 70]. [70] 18

Figure II-8. Schematic of possible polymer/clay composites morphologies. Reprinted with permission from [reference 76].[76] 20

Figure II-9. Schematic of the layer-by-layer (LbL) assembly process. 21

Figure II-10. The corrosion process of steel with water, oxygen, and electrolytes. Reprinted with permission from [reference 88]. [88] 22

Figure II-11. Schematic of self-healing mechanism of capsules loaded with healing agent. Reprinted with permission from [reference 103].[103] 25

Figure II-12. Chemical structure of some ICPs. Reprinted from [reference 113]. [113] 26

Figure III-1. a) Schematic of the PEO/PAA+MMT layer-by-layer process. b) Thickness as a function of bilayers deposited for films with varying MMT concentration and c) FTIR spectra of MMT, PAA, and a 50:50 PAA+MMT mixture. 32

Figure III-2. Atomic force microscope phase images of 10 BL a) PPM [25%] and b) PPM [100%] deposited on silicon. TEM cross-sectional images of 10 BL c) PPM [25%] and d) PPM [100%] deposited on PET. 34

Figure III-3. Schematics of PEO/MMT films assembled a) with and b) without PAA present, and c) hypothesized behavior of the thin film assembled with PAA when applying external strain. 35

Figure III-4. a) Oxygen transmission rate of 10 BL PPM [25%], deposited on polyurethane rubber, after exposure to varying strain. b) Scanning electron microscope surface images of PPM [25%], PPM [50%], and PPM [100%] after exposure to varying levels of strain. 37

Figure IV-1. (a) Schematic representation of CNF/VMT LbL assembly. (b) Thickness of LbL films prepared by using three different CNF concentrations, (c) mass of the thin film, including immobilized liquid, as a function of the number of bilayers deposited and (d) visible light transmission of the thin films as a function of bilayers deposited for the 0.2wt% CNF/VMT system. 45

Figure IV-2. (a-c) Atomic force microscopy (AFM) height images of 3.5 BL CNF/VMT films prepared with varying CNF concentration. (d) Phase image of the film prepared with 0.2 wt% CNF/VMT. (e) Cross-sectional TEM image of a 10 BL 0.2 wt% CNF/VMT film. 46

Figure IV-3. (a) Oxygen transmission rate (OTR) of CNF/VMT films as a function of bilayers deposited. (b) Permeability as a function of thickness of LbL assembled CNF/VMT films in relation to other cellulose-based films: 15 BL and 20 BL are CNF/VMT films from this work, CNF films are from ref ([61]), CNF-2 is from ref ([63]), CNF/MMT is from ref ([155]), MMT/DA-CNF is from ref ([160]), and neat cellulose is from ref ([60]). 47

Figure IV-4. Photographs of (a) foam coated with 2 and 4 BL CNF/VMT (left and right foam, respectively) before burning. Photographs and SEM images of cross sections of PU foam coated with (b) 2 and (c) 4 BL CNF/VMT after torch testing. Boxes of the same color represent the same spot with different magnifications. 50

Figure IV-5. (a) Weight and (b) first derivative weight loss as a function of temperature for uncoated and LbL-coated PU foam. 51

Figure V-1. (a) Schematic of the LbL assembly process. (b) Digital images of $(PU/VMT)_{10}$ coatings deposited on coated on PET (right side of yellow line), uncoated PET (left side of yellow line) and bare aluminum. (c) Cross-sectional TEM image of a $(PU/VMT)_{10}$ coating on PET and schematic of the thin film structure. (d) Growth curves for PU/VMT and PEI/VMT multilayer

coatings. (e) Visible light transmittance as a function of PU/VMT bilayers deposited on quartz slides. 57

Figure V-2. NMR spectra of (a) branched polyethylenimine and (b) polyurethane. (c) The swelling ratio of (PEI/VMT)10 and (PU/VMT)10 coatings in 3.5% NaCl solution. (d) Schematic of ion transport in these LbL assembled films..... 58

Figure V-3. EIS spectra (Nyquist and Bode plots) of (a) $(PU/VMT)_{10}$, (b) $(PU/VMT)_{20}$, (c) $(PU/VMT)_{30}$, and (d) $(PU/VMT)_{40}$ deposited on aluminum, for up to five days in 3.5 wt.% NaCl solution. 60

Figure V-4. Equivalent electrical circuits used to fit the EIS data for bare aluminum and the different polymer-nanoclay composite coatings immersed for five days in 3.5 wt% NaCl solution. 61

Figure V-5. (a) R_p evolution for samples immersed for 5 days in a 3.5 wt.% NaCl solution. (b) Rp values of all samples on Day 5. 62

Figure V-6. SEM (left two columns) and optical microscope (right two columns) images of (a) uncoated aluminum, (b) $(PEI/VMT)_{40}$, and (c) $(PU/VMT)_{30}$ before the EIS test, along with (d) uncoated aluminum, (e) $(PEI/VMT)_{40}$, and (f) $(PU/VMT)_{30}$ after a 5-day immersion in a 3.5% NaCl solution. 65

Figure VI-1. Schematic representation of (a) layer-by-layer assembly of PEM (e.g. PEI/PAA) coatings, (b) physical vapor deposition of SiO_x layers, (c) multilayer thin film preparation with PEM and SiO_x layers. 70

Figure VI-2. (a) Visible light transmission of multilayer thin films based on SiOx and PEM layers. (b) Digital photographs of SiOx+PEM and PEM+SiOx+PEM coated on PET substrate. 71

Figure VI-3. Water vapor transmission rate (WVTR) of various samples coated on 179 μm PET substrate, measurements were conducted at 38°C 90% RH. 72

LIST OF TABLES

Page

Table II-1. Oxygen transmission rate (OTR) of cellulose films in the literature. 15

Table II-2. OTR and WVTR values of inorganic thin film coatings. Reprinted from [reference 68].[68] 17

Table II-3. Oxygen permeability of some polymer/clay composites. Reprinted from [reference 28].[28] 20

Table III-1. Barrier behavior of ten bilayer thin films deposited on 1 mm thick polyurethane rubber. 38

Table IV-1. Oxygen permeability of CNF/VMT coatings on PET (measured at 23 °C and 0% RH). 48

Table IV-2. Torch test results for coated and uncoated polyurethane foam. 49

CHAPTER I

INTRODUCTION

1.1 Background

Protective coatings have been used in various applications such as packaging, flame retardant, and corrosion prevention to safeguard an underlying substrate. Gas barrier is one of the most important properties of protective coatings due to its critical role in packaging, especially for sensitive food and organic electronics.[1-3] Current packaging materials available in the market include metalized plastics, inorganic transparent coatings, polymers, and polymer composites. Due to the disadvantages such as high opacity and difficulty with recycling for metalized plastics, poor adhesion and brittleness for inorganic coatings,[4-6] polymer composites are attracting more attention. In the case of clay-filled composites, random alignment and aggregation of platelets reduce barrier and transparency of the composites, making them unsuitable for many packaging applications. Additionally, packaging waste has become a major environmental burden, creating a need for the development of biodegradable and compostable packaging materials. Protective coatings with good barrier against corrosive species (e.g., oxygen, water, and Cl^-) are also desired in corrosion prevention, since corrosion literally eats up 3% of the world's gross domestic product (GDP) annually.[7] Multilayer anticorrosion coatings are typically used to ensure good protection, with a chromate conversion coating (CCC) as a pretreatment layer due to its excellent barrier and self-healing ability. However, chromate conversion coatings are now restricted or banned in many regions because of health concerns,[8] so more environmentally-friendly replacements for CCCs are needed.

Layer-by-layer (LbL) assembly is one of the most widely used techniques to prepare thin film coatings with multiple functionalities owing to its simplicity and versatility.[9-10] As shown in Figure I-1, a thin film coating is typically assembled by alternately depositing species with opposite charges. Besides electrostatic attraction, other bonding forces such as hydrogen-bonding,[11] covalent bonds,[12] and hydrophobic interactions,[13] can also be utilized to assemble thin films, which provide the ability to integrate a variety of polymers and nanoparticles for desired functionalities. The coating structure can also be precisely tuned by adjusting processing parameters such as temperature,[14] solution pH,[15] number of deposition cycles,[9] ionic strength,[16] and solution concentration.[17] It is for these advantages that LbL assembly shows great potential for gas barrier/separation,[18-19] flame retardant,[20] drug delivery,[21] sensors,[11, 22-25] thermoelectricity,[26] and corrosion protection.[8]

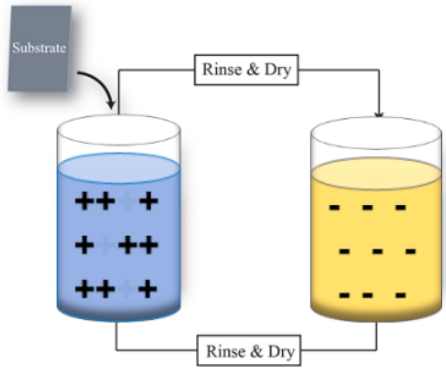

Figure I-1. Schematic of layer-by-layer assembly (LbL) process.

1.2 Dissertation Outline

Chapter II provides an overview of protective coatings, focused on two major applications: gas barrier and corrosion protection. The first part introduces commonly used

oxygen barrier thin films, including inorganic metalized plastics, polymer composites, and transparent metal oxide coatings. A review of layer-by-layer assembly is also included. The second part of the chapter describes corrosion protection coatings, emphasizing corrosion resistance of polymeric coatings.

Chapter III describes a new strategy of designing a stretchable gas barrier to overcome the trade-off between stretchability and barrier. By alternately depositing layers of poly(ethylene oxide) (PEO) and montmorillonite (MMT) clay and poly(acrylic acid) (PAA), with MMT and PAA combined in a single aqueous deposition solution, multilayer films with high clay concentration and alignment were prepared and showed huge improvement in oxygen barrier. A 10 bilayer (BL) PEO/PAA+MMT film deposited on a 1 mm polyurethane rubber substrate results in a 54X oxygen transmission rate (OTR) reduction at 20% strain, and the oxygen permeability is nearly five orders of magnitude lower. This is the best stretchable gas barrier ever been reported, making these films useful for stretchable packaging applications and pressurized systems.

Chapter IV demonstrates the ability of using LbL assembly to improve gas barrier, flame resistance, and mechanical properties of cellulose membranes. Cellulose is considered an inexhaustible source of environmentally-friendly and biocompatible raw materials. Cationically-modified cellulose nanofibrils (CNT) were assembled with anionic vermiculite clay (VMT) for the first time. The highly aligned VMT platelets create nanobrick wall structure that imparts great transparency, improved flame resistance, and oxygen barrier. A 20 BL CNF/VMT nanocoating, with a thickness of only 136 nm, exhibits an OTR as low as 0.038 $cm^3/(m^2$ day atm). With only 2 BL of CNF/VMT, the

melting of flexible polyurethane foam is completely stopped when exposed to a butane torch. This coating also exhibits high elastic modulus and hardness. These LbL assembled multifunctional CNF/VMT coatings shows great potential for biodegradable packaging and protection applications.

Chapter V demonstrates high corrosion resistance with ultrathin transparent nanoscale anticorrosion coatings on aluminum alloy 7075-T651. For the first time, cationic waterborne polyurethane (PU) and anionic vermiculite multilayer films were deposited using layer-by-layer assembly. When compared with polyethleneimine (PEI)/VMT multilayer films, the combination of the more hydrophobic polyurethane and highly aligned clay platelets leads to better barrier properties in an aqueous environment. A 30-bilayer PU/VMT coating, with a thickness of only 300 nm, provides two orders of magnitude improvement in impedance and imparts corrosion protection for five days, which is comparable to other composite coatings that are two orders of magnitude thicker. This study shows a new LbL coating system for an effective, transparent and environmentally friendly pretreatment layer for aluminum alloys.

Chapter VI provides conclusions and outlines two potential future studies. This dissertation demonstrates the effectiveness of LbL coatings, especially polymer-clay multilayer coatings as gas barriers, flame retardant materials, and corrosion protection coatings. Different strategies have been used to incorporate nanoclay platelets into polymeric films, which greatly improve the coating performance. The exploration of new functionalities makes these LbL-assembled coatings more appealing for various applications. Going forward, a stacked multilayer coating is proposed to improve the

moisture barrier of these water-based coatings. Initial results show nearly an order of magnitude improvement in moisture barrier with a three-layer polyelectrolyte/SiO_x/polyelectrolyte coating. The role of each layer has also been investigated to confirm the optimized structure. Another proposed study involves design of a corrosion barrier coating using PEI/Nafion as a topcoat. Preliminary results show that the LbL assembled PEI/Nafion nanoscale coating has a superhydrophobic surface with a very high contact angle due to the hydrophobicity of Nafion and its surface roughness. This coating will be applied on top of a PU/VMT layer, which has already shown good corrosion resistance based on Chapter V, to block the diffusion of water and possibly improve corrosion protection.

CHAPTER II

LITERATURE REVIEW

2.1 Protective Coatings: Gas Barrier

Super gas barrier films are important for food, pharmaceutical, and electronics packaging, as low permeability to gases (e.g., oxygen, and moisture) is desired to extend the life of products.[1-3, 27] Due to low cost, ease of production, and tunable properties of polymers, they are gradually replacing conventional metal and ceramic gas barriers over the past few decades. More than 40% of polymers produced, including polyethylene (PE), polypropylene (PP), polystyrene (PS), polyethylene terephthalate (PET), are used as packaging materials in the form of bottles, boxes, and films.[28] Even so, the intrinsically high permeability of these polymer films limits their ability to protect sensitive food, medicine and electronic displays (e.g., LED). Materials such as metalized plastics and polymer composites are exploited to improve barrier performance.

Although metalized plastics are among the most commonly used packaging materials due to their high barrier and relatively low cost, the lack of transparency and microwaveability (as well as difficulty with recycling) remain problematic.[4] Inorganic barrier coatings, such as SiO_x or Al_xO_y, show good optical clarity and barrier, but poor adhesion and inherent pinholes limit their utility.[5-6] On the other hand, polymer composites can significantly improve barrier by creating higher tortuosity for gas molecules, this will be described in Section 1.2.3. Moreover, biodegradable gas barrier materials (e.g., cellulose and starch) are also being studied to curb carbon emissions and reduce plastic

waste.[27] Different theories regarding gas transmission through thin films will be discussed here along with various gas barrier materials and their corresponding challenges.

2.1.1 Gas Transport Theories

Understanding gas transport through thin film coatings facilitates better design of gas barriers. In general, there are two models that describe gas transport through materials: solution-diffusion and diffusion through impurities (such as defects and pinholes). The solution-diffusion model applies to dense, non-porous polymer films.[29] With the pressure difference across a membrane as a driving force, the gas molecules will dissolve in the membrane, followed by diffusing and desorbing. Diffusion is the rate-controlling process, which depends on the free volume in the polymer membrane. The smaller the free volume, the "tighter" the membrane and the better barrier it has.[30] The permeability coefficient [P] (in mol Pa^{-1} m^{-1} s^{-1}) of a polymer membrane to gas molecules is:

$$P=S*D \tag{1}$$

where S and D are the solubility and diffusion coefficients of that particular gas. The diffusion coefficient is a kinetic factor that depends on the mobility of the gas molecule in a polymer matrix. The solubility coefficient is a thermodynamic factor relating to the interaction between gas and polymer.[31] D obeys a Arrhenius relationship:[29, 32]

$$D = D_0 \exp\left(-\frac{E_D}{RT}\right) \tag{2}$$

where D_o is a front factor and E_D is the activation energy for gas diffusion. The relation between the activation energy and gas molecule size was modeled as follows:[29]

$$E_D = cd^2 - f \tag{3}$$

where c and f are constants that depend on polymer properties and d is the diameter of gas molecules. The constant (c) ranges from around 250 cal/mol Å^2 for flexible poly(dimethyl-siloxane) to 1100 for poly (vinyl chloride). (f/c)½ is related to the average distance between polymer chains.[33] Based on the equations above, the permeability coefficient can be expressed as:[29]

$$\ln P = lnS - \left(\frac{1-a}{RT}\right) cd^2 + f(\frac{1-a}{RT}) - \text{b} \quad (4)$$

where a and b are constants. Equation 4 shows that tuning polymer properties such as backbone stiffness and interchain spacing results in increased c and f, and thereby lowers permeability.

Nelson[34] argued that the preceding model cannot be applied to inorganic films such as silicon or aluminum oxides. For these coatings, the diffusion through pinholes dominates the gas transport, which can be evidenced by the independence of permeability over thickness. In this scenario, the amount of gas molecules transport permeating through defects per unit time can be expressed as:[35]

$$Q = \frac{q_H}{t} = \frac{\pi R_0^2 D\Phi}{L} \quad (5)$$

where R_o is the hole radius, D is the diffusion coefficient, L is the coating thickness and Φ is the gas concentration. The water vapor transmission rate (WVTR) can be expressed as follows:[35]

$$WVTR = \sum_{k=0}^{n} \left(\frac{Q}{A}\right) \text{N} \quad (6)$$

where A is the area of the test sample and N is the number of defects.

For polymer composite thin films, mass transport is usually described by the tortuous pathway model, where the composites consist of a permeable polymer matrix and impermeable nanoplatelets. In this model, the diffusion coefficient D is expressed as:[31]

$$D = \frac{D_0}{\tau} \tag{7}$$

where D_0 is the diffusion coefficient of the polymer matrix and τ is the tortuosity of the system, which is defined as the ratio of distance that a molecule must travel through the membrane reinforced with nanoplatelets over the thin film thickness. Tortuosity is the main factor that influences the permeability of the composites (Figure II-1). When the platelets are aligned parallel to the substrate, τ is given as:[31]

$$\tau = 1 + \frac{L*\phi}{2W} \tag{8}$$

where ϕ, L and W are volume fraction, length and thickness of the nanoplatelets, respectively. This equation shows that increasing volume fraction and aspect ratio decreases the diffusion coefficient and thus reduces permeability. However, for most polymer clay composites, the volume fraction has been limited to no more than 10% due to aggregation and misalignment, which will be discussed in the following section.[31]

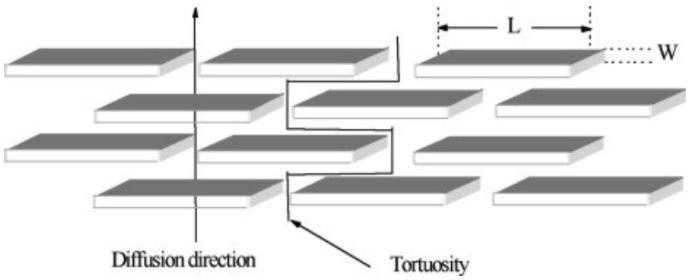

Figure II-1. Schematic of the tortuous pathway in polymer/clay composites. Reprinted with permission from [reference 31].[31]

2.1.2 Gas Barrier Materials

2.1.2.1 Petrochemical and Biodegradable Polymers

The petrochemical-based plastics, that include polyvinylchoride (PVC), polythelyene terephthalate (PET), polyethylene (PE), polypropylene (PP), polystyrene (PS) and polyamide (PA), have been extensively used as packaging materials due to their low cost, relatively good barrier, and good mechanical properties. As discussed earlier, structural factors such as steric hindrance, side-group substitution, and crystallinity affect the gas diffusion within these films. Figure II-2 summarizes the oxygen permeability of commonly used polymer membranes. In general, stiff polymers with high crystallinity and side groups that interact with gas molecules (hydrogen bonding, polar-to-polar interaction) exhibit better barrier.

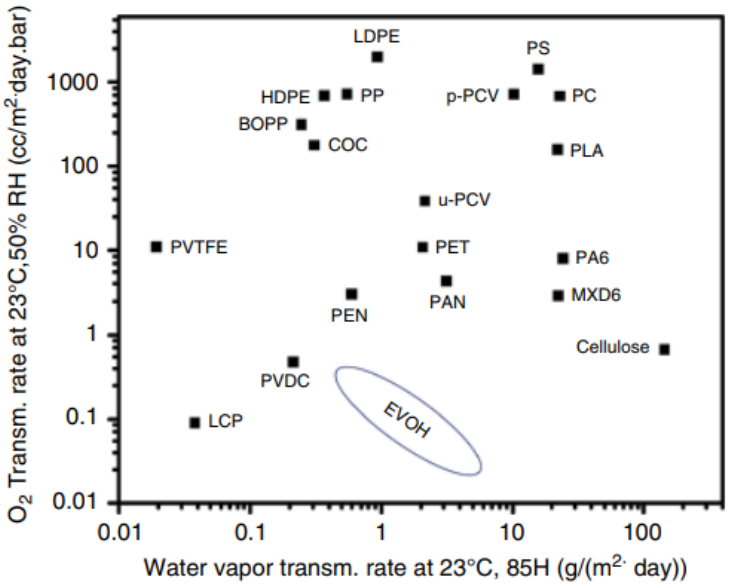

Figure II-2. Oxygen and water transmission rates of commonly used polymers in packaging. Reprinted from [reference 36].[36]

Besides their relatively low barrier, most of the plastic packaging materials are not biodegradable and recycling is usually not economically feasible, especially when contaminated with food or biological substances.[37] More than 5000 Mtons of plastics have been disposed of since 1950, which has become a major environmental burden. This is especially true for the oceans, where the biophysical breakdown of plastics takes place and severely threatens wildlife.[38] There is increasing need for the development of biodegradable and compostable packaging materials. As shown in Figure II-3, these materials work well in the eco-system with certain aerobic and anaerobic microorganisms needed for biodegradation.[39] Current biodegradable materials include petrochemical-based polymers (e.g., certain types of PE and PVA) and bio-based polymers (e.g., poly (lactic acid)[PLA], starch and cellulose).[37] The latter has attracted more attention due to

its renewability and abundance in nature. For example, PLA is a commercial material that has tunable properties, and sometimes outperforms oriented polystyrene (PS) or polyethylene terephthalate (PET).[40] It is typically synthesized with the lactic acid monomer from the fermentation of sugar, corn, etc.[41] And the degradation occurs through hydrolysis that breaks down ester linkages.[37] Starch is another bio-based polymer that has great biodegradability.[37] Since it is thermally unstable, starch is usually used as an additive to accelerate the fragmentation process of oil-based polymers by producing pores that weaken the materials. Starch-polymer blends have been commercialized under trade names such as Ecostar®, Bioplast®, Eco-Foam®, and Enviofill®.

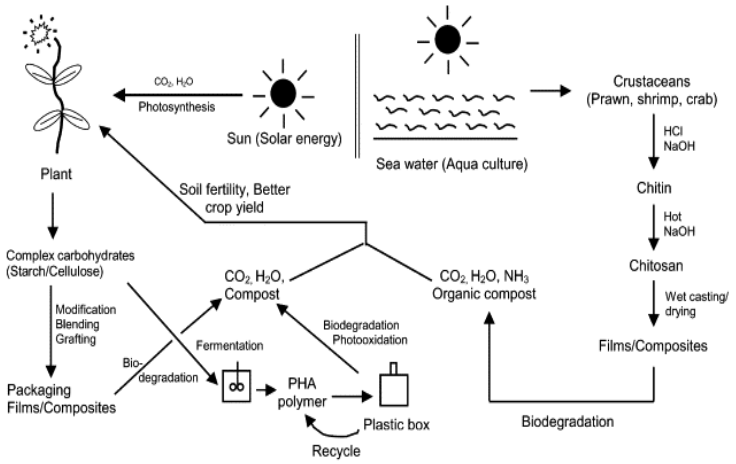

Figure II-3. The life cycle of biodegradable polymers. Reprinted with permission from [reference 39].[39]

Cellulose is the most common, renewable biopolymer, and can be found in the cell walls of wood, cotton, fungi, and algae. The global production of cellulose is estimated to be 10^{11}-10^{12} t/year by photosynthesis.[42] For centuries, cellulose-based materials have been exploited for paper and textiles. In the modern age, while still holding its place in

traditional paper-making and textile industries, cellulose (especially cellulose nanofibrils (CNF)), has been widely studied for applications such as biomedical implants, bio-degradable packaging, and transparent papers.[43-46] Cellulose nanofibrils (CNF) [also denoted as cellulose microfibrils (CMF) or nanofibrilated cellulose (NCF)] is a nanomaterial with a square cross-section area in the range of 25-100 nm^2 and a length up to a few micrometers.[44] It is usually isolated from soft wood pulp, as shown in Figure II-4, with the native degree of crystallinity varying from 40% to 70% depending on the origins and processing methods.[44, 47]

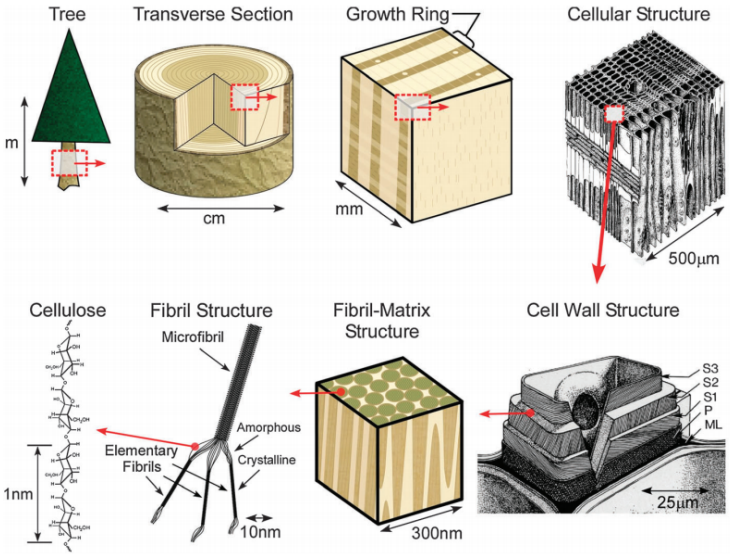

Figure II-4. Schematic of typical process to obtain CNF. Reprinted with permission from [reference 48].[48]

Despite its potential, several problems remain regarding the processability of CNF, which limits the industrial use in spite of its excellent chemical resistance and mechanical properties. One big challenge is the insolubility in water and most organic solvents. Unlike starch, the β-1,4 glucosidic bond in cellulose aligns the macromolecular chains. This

allows the formation of inter/intra chain hydrogen bonds as well as hydrophobic interactions, which results in low solubility.[49-50] Additionally, the isolation of CNF with mechanical disintegration requires high energy (up to 70000 kWh/ton).[51] Finding a way to better isolate and disperse CNF is critical. In recent years, there have been many breakthroughs regarding dispersion and isolation, making it possible for mass production and commercial applications. For example, Saito et al. reported a β-2,2,6,6-tetramethylpiperidine-1-oxyl (TEMPO)-mediated oxidation method that introduced carboxylate and aldehyde functional groups, which allows CNF to be dispersed in water.[52] Other methods such as enzymatic hydrolysis, sulfonation, quaternization, and solvent-assisted pretreatments (Figure II-5) were studied, which reduce energy consumption.[47, 53-55]

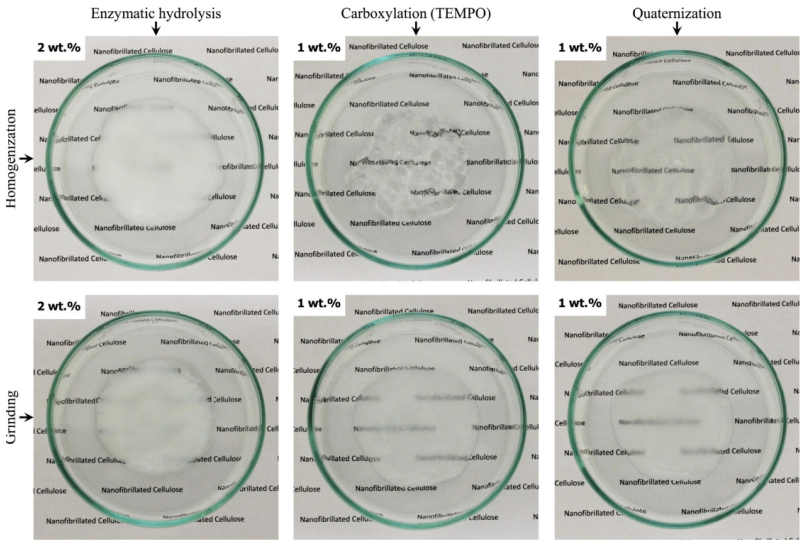

Figure II-5. Digital photographs of pretreated CNF suspensions. Reprinted with permission from [reference 47].[47]

CNF thin films usually feature good optical clarity due to their nanostructure reducing light scattering, high elastic modulus, and low thermal expansion coefficients.[56-59]Various studies are focused on the oxygen barrier of CNF films for biodegradable packaging. Syverud prepared CNF films from suspension and obtained an oxygen permeability of 0.352 (cm^3 mm/m^2*day*atm).[60] Incorporating pretreatment methods into film preparation improves barrier performance. The oxygen permeability was improved to $6*10^{-5}$ (cm^3 mm/m^2*day*atm) at 0% humidity with TEMPO-treated CNF owing to denser film structure as a result of better fibrils isolation.[61] Table II-1 summarizes the oxygen barrier performance of some CNF films reported in literature. Different inorganic fillers such as montmorillonite clay (MMT) have been introduced to the CNF matrix for better barrier,[62] which will be discussed in Section 2.1.2.3.2.

Table II-1. Oxygen transmission rate (OTR) of cellulose films in the literature.

Materials	Oxygen Permeability (cm^3*μm)/(m^2 day kPa)	Condition	Ref
CNF (no pretreatment)	3.52-5.03	23 °C, 50%RH	[60]
CNF(carboxymethylated)	0.85	23 °C, 50%RH	[61]
CNF (carboxymethylated)	0.0006	23 °C, 0%RH	[61]
CNF (NaOH/urea solvent casted)	0.003	23 °C, 0%RH	[63]
CNF(TEMPO-mediated)	0.004	23 °C, 0% RH	[64]

2.1.2.2 Inorganic Coatings

Improved gas barrier can be provided by coating polymer substrates with a thin layer (typically 20-100 nm) of aluminum.[65] Although metal thin films exhibit very high oxygen and moisture barrier at low cost, they are not transparent or microwavable.[4] Transparent inorganic oxide coatings such as silicon or aluminum oxides, however, can

fulfill these requirements. Two major techniques, physical vapor deposition (PVD) and chemical vapor deposition (CVD), are used to deposit thin films. For PVD, Si and O atoms are vaporized from a solid target. And then travel through plasma or a low vacuum environment and condense on the substrate. The products of chemical reaction in the vapor phase are deposited onto a heated surface (>600 °C) during the CVD process.[36]

Although these inorganic coatings have been commercially available for decades, their growth is limited due to their inherent brittleness and poor adhesion to polymer substrates, which cause micro-defects. During the vacuum-deposition process, pinholes and voids can be formed when the substrate is rough or has foreign objects, known as the shadow effect (Figure II-6a).[66] Additionally, nano-defects (e.g., boundaries between the grain-like SiO_x structure) resulting from nonequilibrium thermodynamic nature of the coating process are also observed. These micro-and nano-defects significantly deteriorate barrier. Studies have shown that the diffusion and solubility coefficients of water vapor, measured from vacuum deposited AlO_x, is an order of magnitude higher than the coefficients of crystalline alumina.[67] It has also been reported that the OTR increases with film thickness when it's beyond an optimized value (Figure II-6b). This thickness trend is due to poor adhesion and internal stress that causes more cracks. Table II-2 lists the OTR and WVTR of some inorganic thin film coatings.[68]

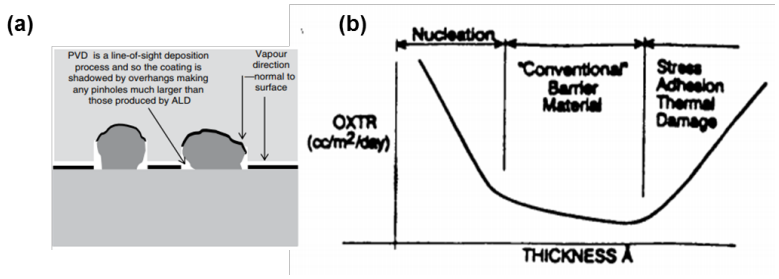

Figure II-6. (a)Schematic of the shadow effect in the PVD process.[36] (b) Oxygen transmission rate (OTR)-thickness relationship.[69] Adapted with permission from [reference 36 and 69].

Table II-2. OTR and WVTR values of inorganic thin film coatings. Reprinted from [reference 68].[68]

Normalized to 1 mil thickness	OTR (cm^3(STP)/m^2 per day per atm)	WVTR (g/m^2 per day) at 90–100% RH	Deposition method
PET/SiO_x a	2.0	1.1	Evaporation
PET/SiO_x c	0.08	0.5	PECVD
PET/AlO_x	1.5	5.0	Evaporation
PET/AlO_xN_y	2.8	4.3	Sputtering
PET/DLC	2	1.5	PECVD
PET/ITO	1.56	0.2	Sputtering
PET/Al	0.31–1.55	0.31–1.55	Evaporation
Nylon/Al	0.8	3.1	Evaporation
PET/7 mm Al foil	0.001	—	Lamination
PET	79	10.7	—

2.1.2.3 Inorganic/Organic Gas Barrier

2.1.2.3.1 Inorganic/Organic Multilayer Films

The rigidity and brittleness of inorganic layers are problematic, especially for applications that require flexibility. Organic layers, on the other hand, are flexible but are usually highly permeable to gas species. Neither materials alone is effective enough to protect organic electronic devices. Combining the two and making inorganic/organic multilayer thin films have proved to be a better option.[70] The well-known Vitex system

for the encapsulation of flexible devices is made of alternating Al_2O_3 and polyacrylate layers (Figure II-7). This technology demonstrated a WVTR of 10^{-6} g/m^2/day.[71-73] The smoothing and defect decoupling effect of the polymer layer, as well as the extended diffusion path, result in a significantly improved barrier in these multilayer films.

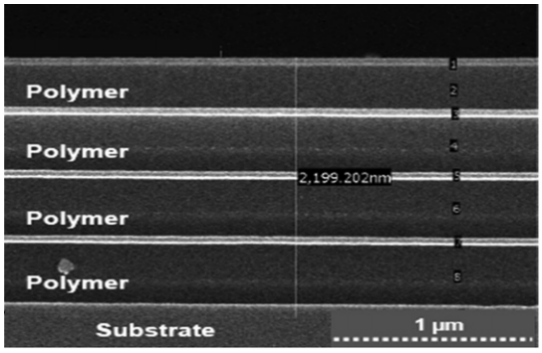

Figure II-7. A cross-sectional scanning electron microscope (SEM) image of four pairs (dyads) of Al_xO_y/polymer multilayer. Reprinted with permission from [reference 70]. [70]

2.1.2.3.2 Polymer/Clay Composites Thin Films

Polymer/clay composites are regarded as a low-cost and effective option for gas barriers. As discussed in Section 1.1, the addition of inorganic fillers (especially platelets) into the polymer matrix improves barrier by creating tortuous pathways. Also, these fillers hinder polymer chain movement and thus decrease the free volume of the film. Among different fillers, natural clay platelets and silicates are usually chosen due to their intercalation ability, low cost and abundancy in nature.[74-75] It can be concluded from the tortuous path model in Section 1.1 that clay characteristics (e.g., aspect ratio and density) and their dispersion properties (e.g., exfoliation and alignment) greatly affect barrier. With that said, achieving good clay dispersion within polymer matrices remains challenging due to the incompatibility between clay and polymer.

Three possible clay morphologies (tactoid, intercalated, and exfoliated) exist within the polymer matrix (Figure II-8), and the oxygen barrier improves as clay dispersion changes from phase-separated tactoids to an exfoliated state.[75-76] Strategies such as surface modification, in situ-polymerization, and solution or melt intercalation have been studied to achieve homogeneous dispersion and improve performance.[75-77] For example, melt intercalation is achieved by mixing and heating up compatible clay platelets and polymers, which helps polymers enter interlayer space and separate clay platelets. More importantly, melt intercalation is compatible with the current techniques such as extrusion and injection molding, making it feasible for industrial-scale production.[78] Surface modification, such as physical adsorption and chemical grafting, or compatibilizers are usually required for intercalation (to increase the interfacial interaction between polymer and clay).[79] The oxygen barrier of some polymer/clay composites is listed in Table II-3. Unfortunately, even with different exfoliating strategies, the clay loading is limited. In the best cases, only 90% barrier improvement can be achieved using clay.[28] Additionally, the random clay alignment in polymer matrix causes low visible light transmission, which is unfavorable for displays.[3]

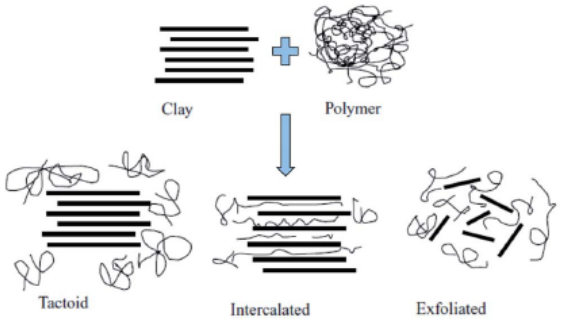

Figure II-8. Schematic of possible polymer/clay composites morphologies. Reprinted with permission from [reference 76].[76]

Table II-3. Oxygen permeability of some polymer/clay composites. Reprinted from [reference 28].[28]

Polymer	Types of clay	Filler loading	Processing [a]	Permeant	Permeability ($m^2\ s^{-1}\ Pa^{-1}$)	Reduction
SBR[18]	O-MMT, CF	16 phr	Melt	O_2	2.75×10^{-17}	46%
PLA[120]	O-MMT	7.9 wt%	Melt	O_2	2.85×10^{-18}	24%
				He	6.79×10^{-17}	23%
PLA, PLA/PCL[121]	O-MMT	3 wt%	Melt	O_2	6.39×10^{-19}	26%
PA[122]	MMT	3 wt%	Melt	O_2	3.37×10^{-19}	14%
				CO_2	1.33×10^{-18}	13%
PET[123]	O-MMT	5 wt%	Melt	O_2	1.69×10^{-19}	55%
PET[124]	O-MMT	5 wt%	Melt	O_2	2.74×10^{-19}	69%
PET[125]	O-MMT	1 wt%	Melt	O_2	1.42×10^{-17}	45%
PS[126]	O-MMT	2 wt%	Melt	O_2	N/A	66%
PP[127]	O-MMT	4 vol%	Melt	O_2	4.18×10^{-18}	46%
PP[128]	O-MMT	7.5 wt%	Melt	O_2	2.59×10^{-15}	56%
PP[129]	MMT, O-MMT	5 wt%	Melt	O_2	$\sim 6.00 \times 10^{-18}$	77%

2.1.3 Layer-by-Layer (LbL) Assembly of Gas Barrier Nanocoatings

Since the pioneering work of Decher and his co-workers,[80] the layer-by-layer assembly (LbL) technique has received lots of attention due to its advantages, such as ease of processing, precise tailorablity, and environmental friendliness.[9] Due to their simplicity and versatility, these thin films have been widely used for a variety of applications including gas barrier and gas separation coatings,[18-19] energy storage and conversion,[81-82] bio-sensors, actuators, and drug delivery.[11, 22-25] Multilayer thin films are prepared by

alternately depositing oppositely charged materials onto a substrate, as shown in Figure II-9. Besides ionic bonds, other forces such as hydrogen bonds, hydrophobic interactions and covalent bonds are also utilized to assemble these films.

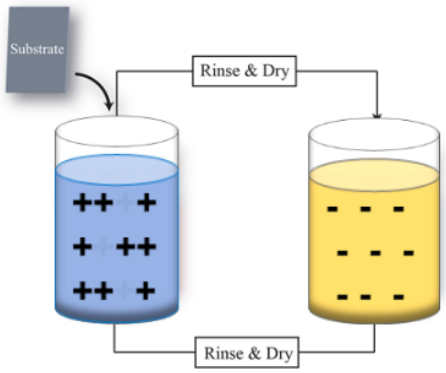

Figure II-9. Schematic of the layer-by-layer (LbL) assembly process.

2.2 Corrosion Protection Coatings

Corrosion consumes 3% of the world GDP.[7, 83] It is a physicochemcial interaction between a metal substrate and its surrounding environment, which could significantly damage the mechanical integrity of the materials. Metals such as aluminum alloy, steel, and copper are prone to corrosion due to their high electrochemical activities.[84-85] During corrosion, oxygen is reduced on the cathodic area of the interface and produces hydroxyl ions, while the oxidation of metal takes place at the anode. For example, Figure II-10 shows the corrosion of steel, which follows the reactions:[86]

$$2H_2O\ (l) + O_2\ (aq) + 4e^- = 4OH^-\ (aq)$$

$$Fe\ (s) = Fe^{2+}\ (aq) + 2e^-$$

The iron hydroxide then undergoes an oxidation reaction into ferrous oxides:

$$6\ Fe(OH)_2\ (aq) + O_2\ (aq) = 4H_2O\ (l) + 2FeO{*}Fe_2O_3{*}H_2O\ (s)$$

In the presence of oxygen, the stable red-brown hydrated hematite ($Fe_2O_3*H_2O$, typically referred as rust) will be formed.[87]

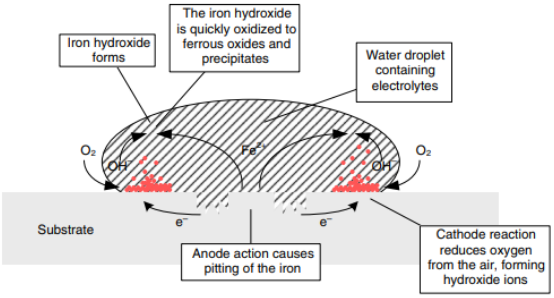

Figure II-10. The corrosion process of steel with water, oxygen, and electrolytes. Reprinted with permission from [reference 88]. [88]

One of the most effective ways to prevent corrosion is to coat the metal. A typical anticorrosion coating system usually consists of a primer, several intermediate layers, and a topcoat.[89] The primer layer ensures good adhesion and provides corrosion protection for the metal substrate, the intermediate layer builds up thickness and thus imparts better barrier against corrosive agents, and the top coat improves resistance to weathering conditions such as ultraviolet radiation.[90] For anticorrosion coatings, there are usually three mechanisms to impede corrosion: barrier protection, corrosion inhibition, and sacrificial protection.[86] Generally speaking, barrier coatings suppress the cathodic reaction by limiting the diffusion of aggressive species (i.e., water, oxygen and aggressive ions) and the transport of electrons on the metal surface. Corrosion inhibitors form insoluble oxides that passivate and protect the surface of metal substrates, while sacrificial coatings provides more electrochemically active components that will corrode first.[91] Barrier and

corrosion inhibition coatings will be the focus of Section 2.1 and 2.2 due to their popularity in corrosion protection.

2.2.1 Chromate Conversion Coatings

Chromate conversion coatings (CCCs) are essentially a combination of barrier protection and corrosion inhibition. They are currently the most effective primer system that provide good corrosion resistance, excellent adhesion and the ability to self-heal.[89, 92] The corrosion inhibition of Cr (VI) involves the formation of insoluble trivalent chromate oxides (Cr_2O_3 or $Cr(OH)_3$) that provide excellent barrier. Meanwhile, the self-healing behavior comes from the reduction of hexavalent chromate (CrO_4^{2-}) to trivalent chromate when exposed to aggressive environments.[93-95] In addition, the adsorption of Cr^{6+} ions on the surface of the metal lowers the zeta potential and hinders the adsorption of corrosive anions. Chromate conversion coatings have significantly increased the corrosion resistance of a variety of aluminum alloys,[90] as well as zinc[96], magnesium[97] have also been reported. Despite the benefits of CCCs, the Cr^{6+} ion is highly water soluble and can pass through cells to damage DNA and cause cancer. [92, 98] As a result, chromate conversion coatings have been a target for regulatory control since 1975 and it has been banned in Europe since 2007.[8] For this reason, environmentally-friendly, high-performance replacements for CCCs are desired.

2.2.2 Alternatives for Chromate Conversion Coatings

2.2.2.1 Hypervalent Transition Metals

One of the ideal replacements for CCCs is reducible hypervalent transition metals (Mo, V, Mn, Tc), which have multiple oxidation states and can be reduced to stable oxides that protect various metals.[99-100] For example, an increase in the corrosion resistance of Al-2024 has been reported with zinc phosphate/molybdate coatings,[89] but the major issue for these coatings is the stability of the oxides at different pH values. Compared with Cr_2O_3, V_2O_3 and MoO_2 are only stable in a very narrow pH range, which compromises their protection in some environments.[90] Although the stability issue can be resolved by using elements such as technetium (Tc), its conversion coating actually outperforms the CCCs for ferrous materials,[92] its radioactivity remains problematic.

2.2.2.2 Polymer-based Coatings

2.2.2.2.1 Self-healing Anticorrosion Coatings

Smart polymeric anticorrosion coatings have been developed to mimic the self-healing behavior of CCCs. Direct doping and loading capsules with corrosion inhibitors are two strategies for these coatings. For direct doping, leaking and undesired interaction between inhibitors and matrices make it disadvantageous in many cases.[101] As a result, studies are focused on distributing nanocontainers that can release healing agents under external stimuli (e.g., pH and temperature) throughout the coatings, as shown in Figure II-11.[102-103]

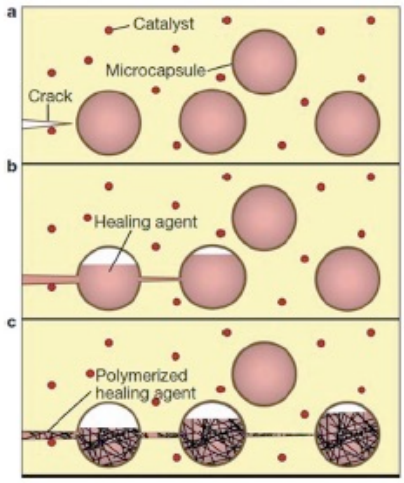

Figure II-11. Schematic of self-healing mechanism of capsules loaded with healing agent. Reprinted with permission from [reference 103].[103]

Polyelectrolyte-based capsules have attracted attention due to the ability to use toward a variety of external stimuli, allowing a controllable release of corrosion inhibitors. Corrosion inhibitors such as 8-hydroxyquinoline, 2-mercaptobenzothiazole (MBT), triethanolamine (TEA) can be used. Once being released from nanocapsules, the inhibitors bond with metal substrates and form a barrier layer.[104-106] For example, benzotriazole-loaded polyelectrolyte nanoreservoirs increased the long-term corrosion protection of a sol-gel coating by forming an insoluble complex between the inhibitor and the metal substrate.[8, 107] It should be noted that the incorporation of nanocontainers can deteriorate the coating due to poor adhesion between capsules and the polymer matrix. Moreover, complex producing limits industrial-scale production of these capsules.

2.2.2.2.2 Intrinsically Conductive Polymers

Since Deberry first reported the anticorrosion performance of polyaniline (PANI) on steel,[108] intrinsically conducting polymers (CPs), including polyaniline, polypyrrole (PPy), polythiophene (PTh), poly(para-phenlyene) (PPP) and polyfuran (PF), have attracted a significant amount of attention.[109-110] Figure II-12 shows the chemical structures of these polymers. Effective corrosion protection has been achieved with the ICPs being in the doped state. The protection mechanism is not yet fully understood, but it is known that the ability to store and transport charge is one of the key factors that facilitates the anodic protection.[111] It has also been suggested that the ICPs help to form a passive oxide layer on the metal surface.[112]

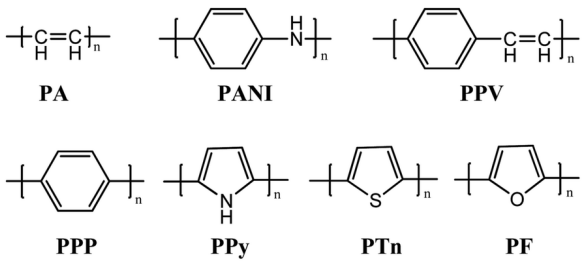

Figure II-12. Chemical structure of some ICPs. Reprinted from [reference 113]. [113]

2.2.2.2.3 Polyurethane Coatings

Polyurethane has been widely used for corrosion protection due to its good mechanical properties, excellent resistance to weathering, and tunable properties.[114-115] These coatings are commercially available as primers or intermediates.[86] It has been reported that a 65 μm thick coating can protect steel for over 250 days because of the combination of high barrier and good adhesion.[114] Owing to regulations that require the reduced usage of volatile organic content, waterborne polyurethane (WPU) has become

more and more popular. The basic components of WPU include diisocyanates, polyols, amines, catalysts and additives, which are also the building blocks for solvent-borne polyurethane.[115-116] Changing the type or structure of these components affects the overall performance of the final polyurethane. Due to the hydrophobicity of polyurethane, emulsifiers are typically required for preparing polyurethane dispersion.[116] When emulsifiers are not effective, hydrophilic ionic functional groups are introduced. Polyols containing carboxylic acid or sulfonic acid can be reacted with isocyanate, to add anionic charge, while the cationic polyurethane is the reaction product of isocyanate prepolymers with amines.[116]

Although WPU are utilized in many applications, it still cannot replace solvent-borne polyurethane for corrosion protection because of its inferior chemical and water resistance.[117] This issue can be resolved with the incorporation of inorganic fillers that improve barrier performance. For example, PU/ZnO coatings prepared with a solvent-blending technique exhibit a 20X higher corrosion resistance on mild steel.[118] Inorganic platelets such as MMT, graphene oxide (GO) have been used and the composites exhibit improved gas barrier and thermal stability that leads to superior protection.[119-120] As mentioned earlier, achieving a highly ordered structure is critical for barrier improvement, so PU/VMT thin films with aligned vermiculite clay have been prepared with LbL assembly. The corrosion protection of these nanocoatings is discussed in Chapter V.

CHAPTER III

COMBINED HIGH STRETCHABILITY AND GAS BARRIER IN HYDROGEN-BONDED MULTILAYER NANOBRICK WALL THIN FILMS*

3.1 Introduction

Although LbL-deposited nanocoatings exhibit especially low gas permeability,[121-123] these nanobrick wall assemblies are typically stiff and cracks develop upon stretching, which damages barrier performance.[124-125] Hydrogen-bonded multilayer thin films are generally less stiff than their ionically-bonded counterparts. The weaker hydrogen bonding creates a looser film structure with lighter crosslink density, enabling greater strain without damage.[126-127] A hydrogen-bonded assembly of poly(ethylene oxide) (PEO) and poly(acrylic acid) (PAA) was recently shown to remain crack free even at 100% strain and PEO/tannic acid maintained its barrier after repeated exposure to 100% strain.[125, 128] Unfortunately, stretchability typically improves at the cost of gas permeability, because the barrier of LbL-deposited films relies upon density, which correlates to stiffness.[129]

In the present work, poly (acrylic acid) and clay were combined in a single deposition solution and alternately assembled with PEO in an effort to further improve gas barrier at high strain. A nanobrick wall structure with homogeneous coverage, high level of alignment, and exfoliation of clay platelets was confirmed with energy-dispersive X-ray spectroscopy (EDS), atomic force microscopy (AFM), and cross-sectional

*Reprinted with permission from Qin, S.; Song, Y.; Floto, M. E.; Grunlan, J. C. Combined High Stretchability and Gas Barrier in Hydrogen-Bonded Multilayer Nanobrick Wall Thin Films. *ACS Applied Materials & Interfaces* **2017,** 9, 7903-7907. Copyright 2017 American Chemical Society.

transmission electron microscopy (TEM). Without PAA in the clay solution (i.e., a PEO/MMT assembly), clay misalignment was observed. A 10 BL PEO/PAA+MMT film (432 nm thick) reduced the OTR of a 1 mm polyurethane rubber substrate more than two orders of magnitude. Unlike ionically-bonded nanobrick wall films, the hydrogen-bonded films are surprisingly stretchable and maintain high barrier at high strain. The 10 BL film reduced the OTR of the PU substrate by nearly two orders of magnitude after being subjected to a 20% strain. This system has the lowest OTR and permeability ever reported at such a high strain. This incredible stretchability is believed to be due to the hydrogen bonding between the PEO/PAA and PAA/MMT interfaces.

3.2 Experimental

Branched polyethylenimine (PEI) (Mw = 25,000 g/mol) and poly(acrylic acid) (PAA) (Mw = 100,000 g/mol, 35 wt % aqueous solution) were purchased from Sigma-Aldrich (Milwaukee, WI). Poly(ethylene oxide) (PEO) (Mw = 4,000,000 g/mol) was purchased from Polysciences (Warrington, PA). Natural sodium montmorillonite (MMT) clay was purchased from Southern Clay Products, Inc. (Gonzales, TX). All chemicals were used as received. Deionized (DI) water (Milli-Q, Billerica, MA) with a specific resistance greater than 18 MΩ was used in all solutions and rinses.

Single-side-polished, 500 μm thick silicon wafers (University Wafer, South Boston, MA) were used as substrates for profilometry and atomic force microscopy (AFM). Polyurethane (PU) rubber (0.762 mm thick, McMaster-Carr, Atlanta, GA) was used as the substrate for oxygen transmission rate (OTR) testing and scanning electron

microscopy (SEM). A 179 μm Melinex ST505 polyethylene terephthalate (PET) film (Tekra, New Berlin, WI) was used as the substrate for transmission electron microscopy (TEM) image. The PU rubber was rinsed with DI water and methanol before use. It was then dried and plasma-treated in order to improve adhesion of the first PEI layer. Polished Ti/Au crystals, with a resonance frequency of 5 MHz, were purchased from Maxtek, Inc. (Cypress, CA), and used to measure mass per layer of nanocoating deposited with a quartz crystal microbalance (QCM).

An aqueous solution of 0.1 wt % PEO was prepared by diluting as-received PEO with DI water. MMT powder was mixed with PAA at specified solid mass ratios (Table S1) and then diluted with DI water to make a total solids concentration of 1wt%. All solutions were rolled for at least 12 h after mixing to achieve homogeneous dispersion. The pH of all solutions was adjusted to 2.5 with 1.0 M HCl. A substrate was first dipped into an aqueous 0.1wt% PEI solution for 5 min, followed by rinsing and drying with DI water and filtered air for 30 s, respectively. The substrate was then dipped into an MMT+PAA solution (or simply a 1 wt% MMT suspension) for another 5 min and rinsed with pH 2.5 DI water three times for 30 s each, in order to protect the pH-sensitive hydrogen bonds between deposited layers. After the deposition of the initial bilayer, alternate 1 min dipping in MMT+PAA and PEO solutions took place until the desired number of bilayers (BL) were deposited. All films were prepared using home-built robotic dipping systems.[130-131]

A P-6 profilometer (KLA-Tencor, Milpitas, CA) was used to measure film thickness on silicon wafers every two deposition cycles. Deposited mass of each layer was

characterized with a research QCM (Inficon, East Sycrase, NY). The 5 MHz quartz crystal was plasma-treated and alternately dipped into each solution. After each deposition, crystals were rinsed with pH 2.5 DI water and left on the microbalance to stabilize for 5 min. Thin film topography was analyzed with an AFM (Bruker Instruments, Billerica, MA). The OTR of thin films, with a thickness near 500 nm, were tested by MOCON (Minneapolis, MN) using an Oxtran 2/21 ML instrument at 0% RH for 120 h. An Instron model 4411 tensile tester (Instron, Norwood, MA) was used to apply different strains to the polyurethane with and without nanocoatings for 2 min. Films were imaged using a JEOL JSM-7500F SEM (JEOL Ltd.,Tokyo, Japan). TEM samples were deposited on PET substrates and then embedded in Epofix resin (EMS, Hatfield, PA). After overnight curing, the samples were cut with an Ultra 45° diamond knife (Diatome, Hatfield, PA). Thin sections (~100 nm thick) were collected and imaged using a Tecnai G2 F20 (FEI, Hillsboro, OR) operated at 200 kV. Fourier transform infrared spectroscopy (FTIR) (Bruker Alpha, Billerica, MA) was used with air as the background. A 1 wt% PAA solution, 1 wt% MMT solution and a mixture of 1 wt% PAA and 1 wt% MMT solution were each dried at 50 °C for 8 hours. The solid residue was then collected for testing. Scan resolution was 2 cm^{-1} and a minimum of 64 scans were signal averaged for each sample.

3.3 Results and Discussion

Barrier films were deposited layer-by-layer onto the polyurethane with 0.1 wt% PEO and 1 wt% PAA+MMT solutions adjusted to pH 2.5 (Figure III-1a). The reason for choosing pH 2.5 for assembling is that it yields the thickest PEO/PAA film.[125] Varying

the MMT:PAA ratio in the aqueous deposition solution was evaluated (keeping total solids at 1 wt%). The prepared PEO/PAA+MMT films are denoted as PPM [X%], where PPM represents PEO, PAA, and MMT. [X%] is the weight percent solids of MMT in the 1 wt% PAA+MMT deposition solution.

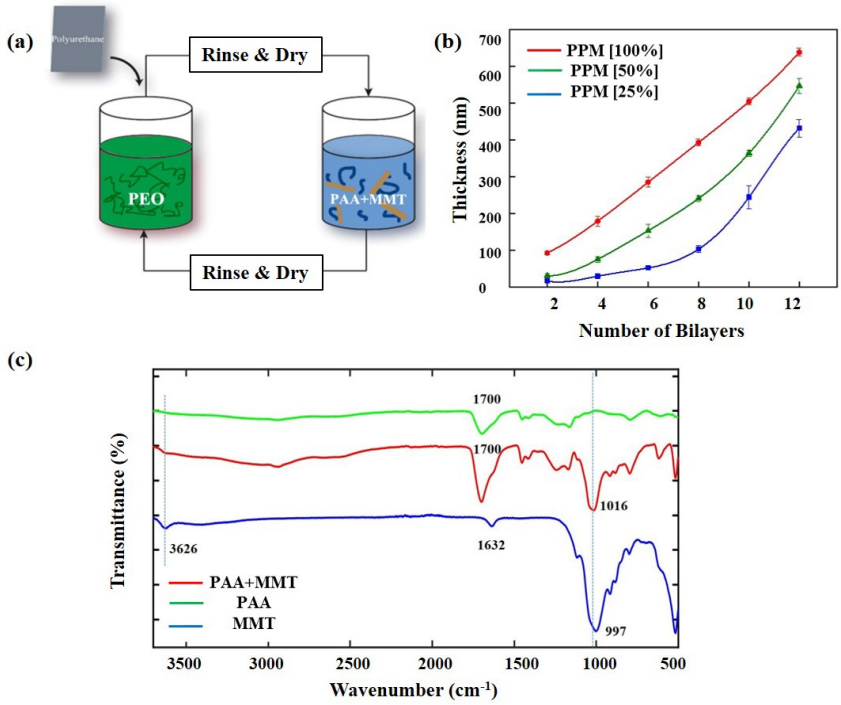

Figure III-1. a) Schematic of the PEO/PAA+MMT layer-by-layer process. b) Thickness as a function of bilayers deposited for films with varying MMT concentration and c) FTIR spectra of MMT, PAA, and a 50:50 PAA+MMT mixture.

Films containing clay, polyethylene oxide and poly(acrylic acid) were assembled on silicon wafers to monitor film growth as a function of the number of bilayers deposited. Figure III-1b shows exponential growth for PPM [25%] and PPM [50%], while the PPM [100%] system grows linearly due to the absence of PAA. Similar growth patterns are observed with a quartz crystal microbalance (QCM), which measures the weight of

deposited layers. The "in-and-out" interlayer diffusion of PAA within these films contributes to the observed exponential growth.[132-133] When the chain mobility is insufficient for interlayer diffusion during the deposition, films grow linearly.[134] This explains the changes in growth pattern as a function of clay concentration, with increasing clay concentration limiting the mobility of PAA.

When MMT is dispersed in pH 2.5 water it aggregates and ultimately settles out of solution because of the house-of-cards structure it adopts.[135] When dispersed in PAA solution, a stable light brown suspension is formed due to the interaction between polymer and clay, which is observed in FTIR spectra (Figure III-1c). The spectrum of MMT alone exhibits Si-OH stretching vibrations at 3626 cm^{-1}, Si-O stretching vibrations at 997 cm^{-1}, and H-O-H bending vibrations at 1642 cm^{-1}. The sharp peak at 1700 cm^{-1} for PAA containing samples is attributed to the C=O stretching vibration of –COOH groups. In the spectrum of PAA+MMT, there is a shift and intensity reduction of the Si-O peak (from 973 cm^{-1} to 1016 cm^{-1}) and reduced intensity of the Si-OH peaks at 3626 cm^{-1}. This interaction is believed to be the hydrogen bonding between PAA and MMT.[136-137] The interaction between PAA and MMT has been well-studied.[136-141] It was observed that the clay adsorbs PAA from aqueous solution and forms intercalated PAA/MMT that facilitates clay dispersion and exfoliation.[141] As a result, MMT platelets remain stably suspended in PAA solution at pH 2.5.

During layer-by-layer deposition, hydrogen bonds are formed between PAA and PEO. With the help of adsorbed PAA, the MMT nanoplatelets are homogeneously incorporated into the multilayer films. Uniform clay dispersion can be seen in EDS

images. AFM images show varying topography with and without PAA. As shown in Figure III-2a, the film with PAA (i.e., PPM [25%]) is relatively featureless, which suggests the clay platelets are fully embedded in the polymer matrix. The topography is very similar for the PPM [50%] film. In Figure III-2b, clay platelets are easily recognized, with similar topography to ionically-bonded PEI/MMT films.[142] Clay misalignment can also be observed in this PPM [100%] film (Figure III-2d), which leads to a rougher surface. Height images of PPM [25%], PPM [50%], and PPM [100%] on silicon wafers have root-mean-square (RMS) surface roughness of 47.2 nm, 54.9 nm, and 70.2 nm, respectively. The decreasing surface roughness with increasing PAA content suggests better alignment of clay platelets in the film.

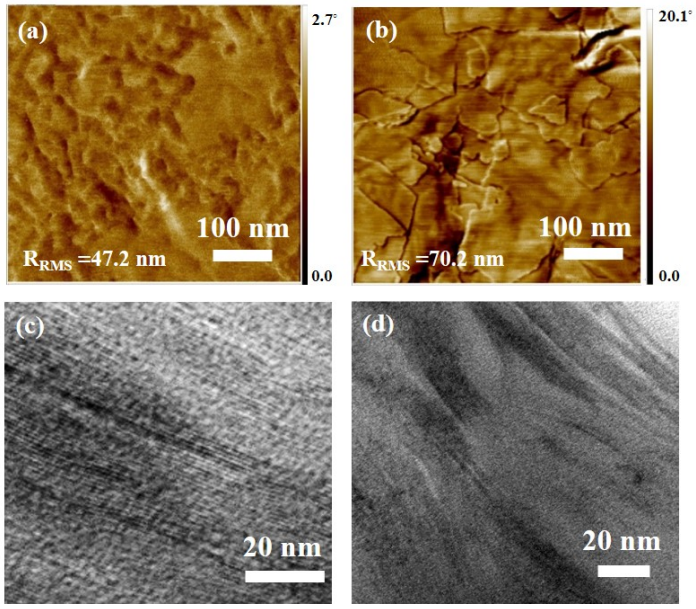

Figure III-2. Atomic force microscope phase images of 10 BL a) PPM [25%] and b) PPM [100%] deposited on silicon. TEM cross-sectional images of 10 BL c) PPM [25%] and d) PPM [100%] deposited on PET.

Clay alignment in these multilayer films is more clearly observed using cross-sectional TEM images of 10 BL films deposited on PET. As shown in Figure III-2c, individual MMT platelets are the dark parallel lines in the PPM [25%] film, revealing a well-ordered nanobrick wall structure that is typical for ionically-bonded polymer/clay assemblies.[121, 142] Platelet stacking and misalignment is observed in the PPM [100%] film (Figure III-2d), which is the likely cause of its greater thickness. Figure III-3 shows schematics of these two different film structures. High levels of clay orientation are only observed in films containing PAA (Figure III-3a), demonstrating the critical role this anionic polymer plays in building the hydrogen-bonded nanobrick wall structure. PAA acts to first stabilize and then separate the MMT platelets in the pH 2.5 solution. The platelets are then incorporated in an aligned structure in the PEO/PAA multilayer film.

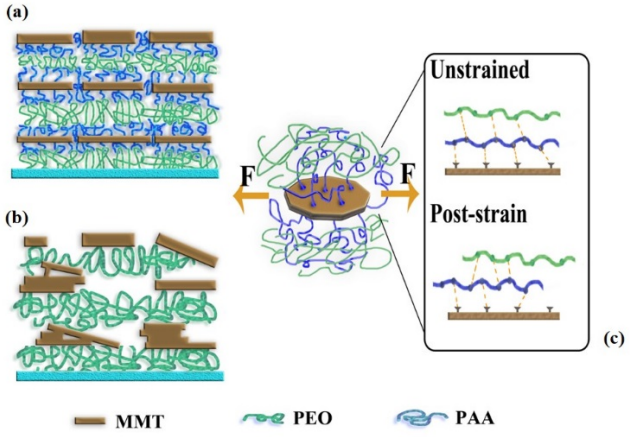

Figure III-3. Schematics of PEO/MMT films assembled a) with and b) without PAA present, and c) hypothesized behavior of the thin film assembled with PAA when applying external strain.

The hydrogen-bonded brick wall nanostructure in these films serves to reduce the oxygen transmission rate (OTR) by creating an extremely torturous pathway for permeating molecules. Figure III-4a shows the OTR of the PEO/PAA+MMT multilayers, each with a thickness of ~500 nm. The transmission rate is nearly an order of magnitude lower than a 20 BL PEO/PAA film that obtained 10X OTR reduction on natural rubber.[125] A 10 BL PPM [25%] film reduces the OTR of a 1 mm thick PU rubber substrate by a factor of 80. PPM [50%] reduces OTR by more than 100X. This improved oxygen barrier is likely due to higher MMT concentration, based upon EDS measurement (data not shown). As expected based on structural analysis, PPM [100%] has the worst barrier among the three films evaluated, despite having the highest MMT concentration. Figure III-3b highlights the large gaps between MMT platelets that are caused by clay misalignment and act as oxygen transmission highways that increase permeability. Scanning electron microscopy (SEM) was used to image each film's surface before and after applying strain (Figure III-4b). The texture observed at 0% strain (for all samples) comes from the polyurethane substrate. For PPM [25%], no cracks are observed up to 20% strain. When stretched 20%, cracks perpendicular to the stretch direction appear in PPM [50%] and PPM [100%], which makes PPM [25%] the best candidate for a truly stretchable gas barrier.

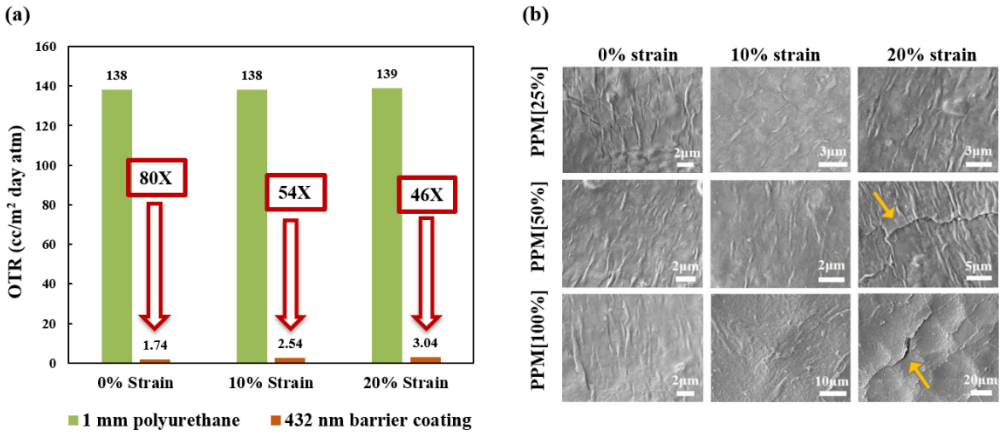

Figure III-4. a) Oxygen transmission rate of 10 BL PPM [25%], deposited on polyurethane rubber, after exposure to varying strain. b) Scanning electron microscope surface images of PPM [25%], PPM [50%], and PPM [100%] after exposure to varying levels of strain.

A 10 BL, 432 nm thick PPM [25%] film exhibits 54 and 46X OTR reduction after 10% and 20% strain, respectively, relative to an uncoated 1 mm PU substrate (Figure III-4a). The permeability of PPM [25%] remains almost five orders of magnitude lower at both 10% and 20% strain. This appears to be the lowest OTR and permeability even reported for a gas barrier thin film after 20% strain. The previous best system maintained a 10X reduction on the same substrate.[143] This superior oxygen barrier after high strain is believed to be due to the hydrogen-bonded nanobrick wall structure. When exposed to external strain, the bond-slip and reorientation along the PEO/PAA and PAA/MMT interfaces reduce the strain felt by the thin film (Figure III-3c).[144] When there are more clay platelets present, they constrain polymer chain motion and reduce the stretchability of the nanocoating. As a result, the PPM [50%] film exhibits greater barrier loss with strain, yielding only 16 and 17X OTR reduction at 10% and 20% strain, respectively. It is

worth noting that the loss of barrier from 0% to 20% strain for PPM [25%] is similar to that of the PEO/PAA film,[125] demonstrating that the incorporation of some amount of MMT clay platelets can improve the gas barrier without compromising stretchability. The barrier properties of these 10 BL films are summarized in Table III-1. Barrier behavior of ten bilayer thin films deposited on 1 mm thick polyurethane rubber..

Table III-1. Barrier behavior of ten bilayer thin films deposited on 1 mm thick polyurethane rubber.

System	Strain	OTR (cc/m^2 day atm)	Thickness (nm)	Permeability (10^{-16} cm^3*cm/cm^2*Pa*s)	
				Total	Coating [±]
PU substrate	0%	138	-	1200	-
	10%	138	-	1200	-
	20%	138	-	1200	-
PPM [25%]	0%	1.74	432	15	0.02
	10%	2.54	432	22	0.03
	20%	3.04	432	26	0.03
PPM [50%]	0%	1.29	549	11	0.02
	10%	8.11	549	71	0.11
	20%	8.43	549	73	0.11

[±]Thin film permeability decoupled from the PU substrate was calculated using a previously described method.[145]

3.4 Conclusions

In conclusion, a highly stretchable gas barrier nanocoating was obtained by successfully incorporating highly aligned clay platelets in a hydrogen-bonded PEO/PAA multilayer assembly. A 432 nm thick, 10 BL PPM [25%] film deposited on 1 mm PU exhibits 80, 54 and 46X OTR reduction at 0%, 10%, and 20% strain, respectively, and retains a permeability five orders of magnitude lower than that of the rubber substrate.

This is the best barrier ever reported for a transparent polymeric coating exposed to such a high strain. This incredible oxygen barrier at high strain comes from the unique hydrogen-bonded brick wall nanostructure, making these films well-suited for applications requiring gas barrier for elastomeric substrates (e.g., balloons, tires, seals, etc.).

CHAPTER IV

SUPER GAS BARRIER AND FIRE RESISTANCE OF NANOPLATELET/NANOFIBRIL MULTILAYER THIN FILMS*

4.1 Introduction

Cellulose nanofibrils (CNF) have attracted tremendous attention because of their colloidal stability, mechanical strength, high specific surface area and thermal stability,[44-45, 146-149] which have been used to produce transparent paper, biodegradable packaging, complex aerogels and as the reinforcing phase in composites.[43-46] Despite all of its beneficial properties, cellulose exhibits poor flame resistance and gas barrier properties.[150-151] Clays have been used as a reinforcing agent in cellulose-based films to improve properties.[152-154] Various methods to increase the interaction between clay and cellulose have been reported, including TEMPO-oxidation and by adding poly(vinyl alcohol) or chitosan as a compatibilizer.[155-157] Recently, cationic CNF with a quaternary ammonium functionality has been studied.[158] It was shown that the ionic interaction between the cationic CNF and clay results in better mechanical properties of the composite, but further improvement is limited due to the formation of nanovoids as well as relatively low clay loading.[153, 158]

---

*Reprinted with permission from Qin, S.; Pour, M. G.; Lazar, S.; Köklükaya, O.; Gerringer, J.; Song, Y.; Wågberg, L.; Grunlan, J. C. Layer-by-Layer Assembly: Super Gas Barrier and Fire Resistance of Nanoplatelet/Nanofibril Multilayer Thin Films *Advanced Materials Interfaces* **2019**, 6, 1970009.

In the present study, multilayer films consisting of anionic vermiculite clay (VMT), with a high aspect ratio (~2000), and cationic cellulose nanofibrils were investigated. The combination of highly aligned VMT platelets and cellulose nanofibrils forms a nanobrick wall structure with high transparency, excellent oxygen barrier and fire resistance. A 20 bilayer (BL) CNF/VMT nanocoating, with a thickness of 136 nm, exhibits a low oxygen transmission rate (OTR) of 0.013 cc/(m^2 day atm). With only 2 BL of CNF/VMT, the melting of flexible polyurethane (PU) foam is prevented when exposed to a butane torch flame. These nanocoatings also exhibit high elastic modulus and hardness. This study demonstrates the useful multifunctionality of these renewable cellulose-based coatings, making them good candidates for packaging and flame protection.

4.2 Experimental

Vermiculite clay (VMT) (Microlite 963^{++}) was purchased from Specialty Vermiculite Corp (Cambridge, MA). The cationic CNF was prepared from quaternized pulp fibers. The cationization was performed following a previously described procedure.[54] A CNF gel was prepared with a 2 wt% suspension of cationic fibers in deionized water. The suspension was homogenized using a high pressure homogenizer (Microfluidizer M-110EH, Microfluidics Corp). A semi-transparent hydrogel was obtained after a single pass through the larger chamber (200 μm) and six passes through the smaller chamber (100 μm). Deionized (DI) water (Milli-Q, Billerica, MA) with a specific resistance greater than 18 MΩ was used in all solutions and rinses. Single-side-polished, 500 μm thick silicon wafers, purchased from University Wafer (South Boston,

MA), were used as substrates for profilometry and atomic force microscopy (AFM). A 179 μm Melinex ST505 polyethylene terephthalate (PET) film (Tekra, New Berlin, WI) was used as the substrate for transmission electron microscopy (TEM) and gas barrier measurement. Polished Ti/Au crystals purchased from Maxtek, Inc. (Cypress, CA), with a resonance frequency of 5 MHz, were used with the quartz crystal microbalance (QCM).

CNF dispersions were prepared by diluting the cationic CNF hydrogel with DI water using tip sonication. A 1 wt% VMT dispersion was prepared through dilution of a 7.5 wt% dispersion using DI water. All dispersions were sonicated and placed on a roller overnight to ensure homogeneity and were used at their unaltered pH. Films were prepared by dipping a given substrate into the CNF dispersion for 5 min, followed by dipping into the VMT dispersion for another 5 min. Substrates were spray rinsed and blow dried between each dipping step. 1 min dipping time was used after the initial bilayer was deposited. All films were prepared using home-built robotic dipping systems.[130-131] For deposition on PU foam, a 10.16 × 10.16 × 2.54 cm^3 piece was cut, rinsed in DI water and then dried at 70 °C overnight. The dried PU foam was submerged for 5 min in a 1wt% polyacrylic acid (PAA) solution that was adjusted to pH 2.0 using nitric acid prior to deposition. This treatment gives the PU foam a negatively-charged surface. After that, the sample was wrung out with a mechanical roller and rinsed by soaking and compressing in DI water. The foam was then immersed in a 0.2 wt% CNF dispersion for 5 min, followed by wringing out with a mechanical roller and rinsing with DI water. The sample was then exposed to the vermiculite suspension in the same fashion to finish the initial bilayer. 1 min immersion time was then applied for the remaining deposition cycles. In each

adsorption step, the foam was compressed three times by hand to ensure the solution uptake into the foam. The coated foam samples were finally heated in an oven at 70 °C until dry.

Film thickness was measured with a P-6 profilometer (KLA-Tencor, Milpitas, CA). A research quartz crystal microbalance (QCM, Maxtek, Sante Fe Springs, CA) was used to measure the mass gain during each layer deposition. Thin film topography was imaged with an atomic force microscope (AFM) (Bruker Instruments, Billerica, MA). The oxygen transmission rate (OTR) was tested by MOCON AMETEK (Minneapolis, MN) using an Oxtran 2/21 ML instrument at 0% RH for 120 h. Films for TEM imaging were deposited on 179 μm PET and then embedded in epoxy resin (EMS, Hatfield, PA). The samples were trimmed and cut with an Ultra 45° diamond knife (Diatome, Hatfield, PA). Thin sections were then collected and imaged using a Tecnai G2 F20 (FEI, Hillsboro, OR) operated at 200 kV. Foam flammability was evaluated by exposure to the flame from a butane micro torch (Model ST2200, Benzomatic, Huntersville, NC) for 10 s (the approximate blue flame temperature is 1300 °C). The thermal stability of the uncoated and LbL-coated polyurethane foam were examined under nitrogen atmosphere using a Mettler-Toledo Thermogravimetric Analyzer (TGA) (Columbus, OH). The samples were 6-10 mg in size and were heated to a temperature of 800°C at a heating rate of 10 °C/min. Mechanical properties were measured using a nanoindenter (Triboscope (TS) 75, Hysitron Inc., Minneapolis, MN), where the maximum load and displacement are 100 μN and 60 nm, respectively. A diamond Berkovich tip (i.e., three-sided pyramid) was used for indentation.

4.3 Results and Discussion

4.3.1 Thin Film Structure

Cationically functionalized cellulose nanofibrils were prepared by introducing quaternary ammonium groups to cellulose fibers before they were subjected to homogenization to liberate the fibrils.[54, 158] The zeta potential of a 0.2 wt% quaternized CNF dispersion is ~57 mV, which indicates a highly cationic surface. Figure IV-1a shows a schematic of the CNF/vermiculite film assembly procedure. The multilayer build-up of the CNF/VMT films, as a function of bilayers deposited on a silicon wafer, is shown in Figure IV-1b. CNF dispersions of 0.05, 0.1, and 0.2 wt% were investigated. Due to the presence of quaternary ammonium groups, for which the charge density is pH-independent, the CNF dispersions were used at their unaltered pH (~7). The use of higher CNF concentration leads to formation of thicker films, which may be ascribed to the greater amount of CNF adsorption, which in turn is linked to the structure of the CNF at the interface. At higher concentrations, the CNF will not deposit as single particles the closer they get to the surface, but in a more associated state.[159] As shown in Figure IV-1b, the film thickness increases linearly as a function of bilayers deposited. This linear growth behavior is also observed in QCM measurements (Figure IV-1c), where the same weight gains (including immobilized liquid) can be observed for each CNF layer. The film density is calculated to be 2.4 g/cm^3 with 70 wt% clay loading. High optical transparency of CNF/VMT films can be observed in Figure IV-1d.

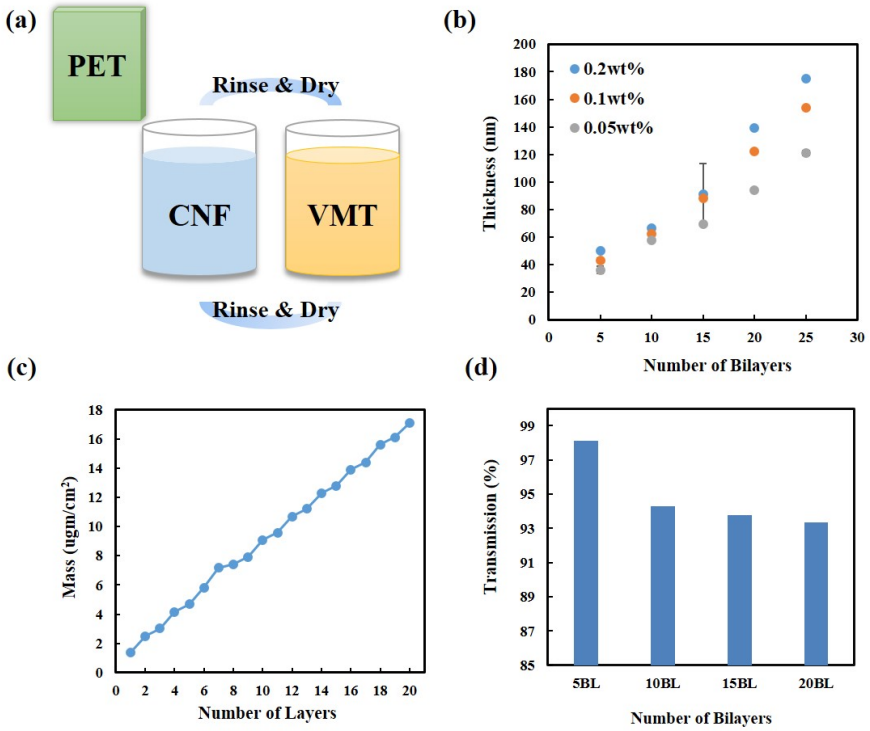

Figure IV-1. (a) Schematic representation of CNF/VMT LbL assembly. (b) Thickness of LbL films prepared by using three different CNF concentrations, (c) mass of the thin film, including immobilized liquid, as a function of the number of bilayers deposited and (d) visible light transmission of the thin films as a function of bilayers deposited for the 0.2wt% CNF/VMT system.

Atomic force microscopy was used to image the surface morphology of the films deposited on silicon wafers. As shown in Figure IV-2, a uniform coverage by CNF can be observed on the film surfaces, with clay platelets lying underneath. It seems that lower CNF dispersion concentration results in a smaller amount of CNF in the film. It is worth mentioning that when the coating is terminated with a clay layer, no CNF can be observed (image not shown), indicating excellent clay coverage. Nanocoatings prepared with 0.2 wt% CNF were further investigated here due to having the greatest thickness per layer. A high degree of clay alignment is achieved in these LbL assembled CNF/VMT films. Cross-

sectional TEM images, where individually deposited vermiculite platelets appear as dark lines as a result of higher electron density, highlight the typical nanobrick wall structure of these CNF/clay assemblies.[121, 142] The thickness measured from TEM images is consistent with the growth curve in Figure VI-1b. The high optical transparency observed can be attributed to the high level of clay alignment and separation (Figure IV-1d).

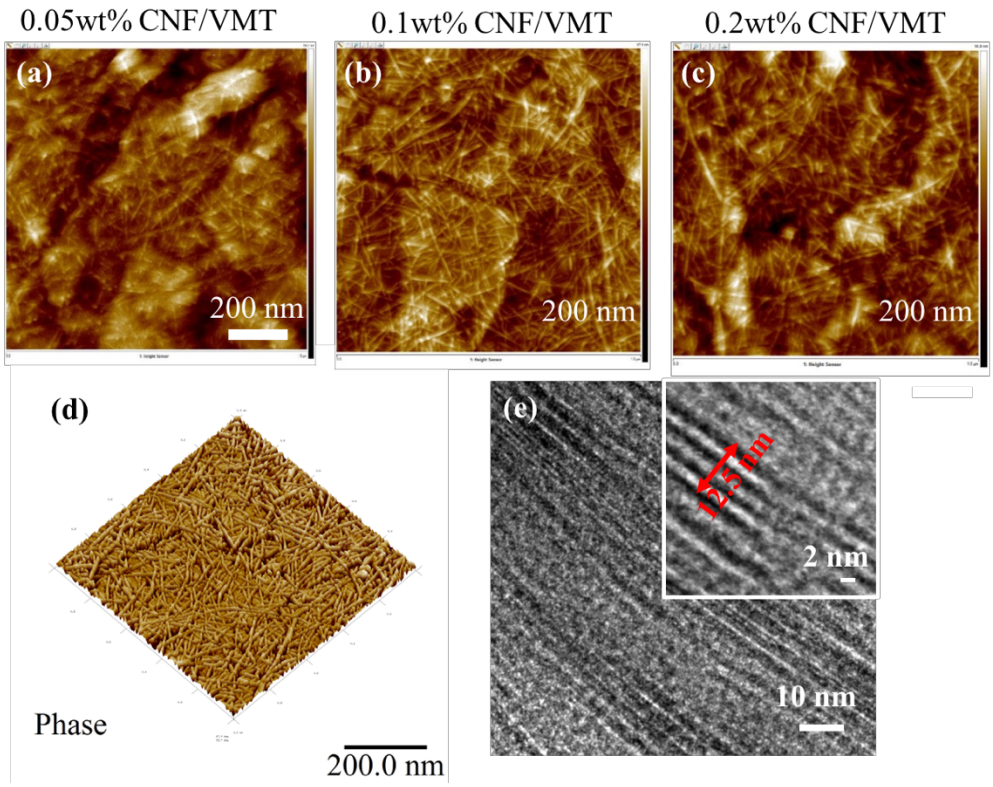

Figure IV-2. (a-c) Atomic force microscopy (AFM) height images of 3.5 BL CNF/VMT films prepared with varying CNF concentration. (d) Phase image of the film prepared with 0.2 wt% CNF/VMT. (e) Cross-sectional TEM image of a 10 BL 0.2 wt% CNF/VMT film.

4.3.2 Oxygen Barrier of Nanocoatings on Polyester

Figure IV-3a shows the oxygen transmission rate (OTR) of the CNF/VMT coatings as a function of bilayers deposited on179 µm thick PET film measured at 23 °C

and 0% RH. The oxygen permeability was calculated and is reported in Table IV-1. A 20 BL film, with a thickness of only 136 nm, reduced the OTR of the uncoated PET substrate by more than two orders of magnitude, from 8.6 to 0.013 cc/(m^2 day atm). The oxygen transmission rate and permeability decrease exponentially with film thickness, which is unique to these LbL assembled films.[3] The oxygen permeability of the 20 BL CNF/VMT coating (4.06×10^{-21} cm^3 cm/ (cm^2 s Pa)) is the lowest ever reported for a nanoscale cellulose-based film. A comparison with other cellulose-based gas barrier coatings is shown in Figure IV-3b. This excellent oxygen barrier is a result of highly aligned clay platelets, which create an extremely tortuous diffusion path and a dense film structure (Figure IV-2e).

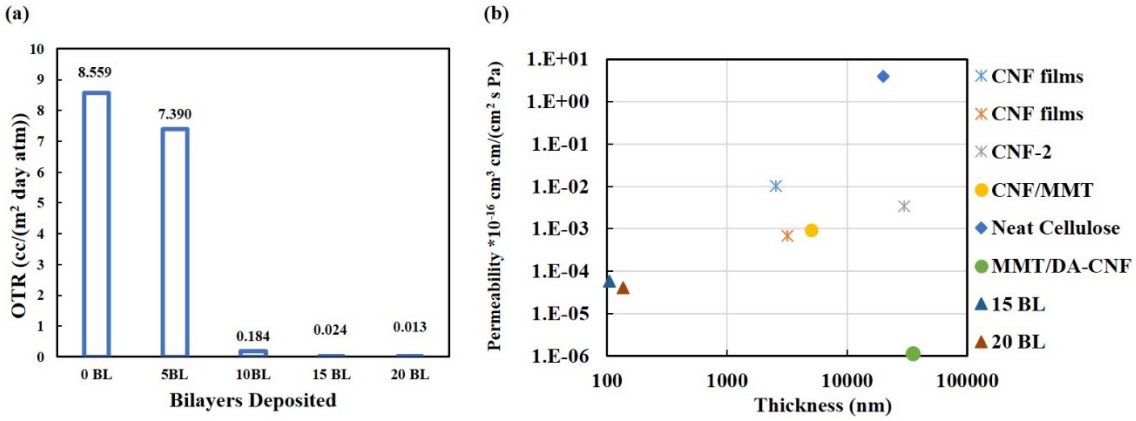

Figure IV-3. (a) Oxygen transmission rate (OTR) of CNF/VMT films as a function of bilayers deposited. (b) Permeability as a function of thickness of LbL assembled CNF/VMT films in relation to other cellulose-based films: 15 BL and 20 BL are CNF/VMT films from this work, CNF films are from ref ([61]), CNF-2 is from ref ([63]), CNF/MMT is from ref ([155]), MMT/DA-CNF is from ref ([160]), and neat cellulose is from ref ([60]).

Table IV-1. Oxygen permeability of CNF/VMT coatings on PET (measured at 23 °C and 0% RH).

BL deposited	OTR (cc/(m^2 day atm))	permeability (10^{-16} cm^3 cm/(cm^2 s Pa))	
		film [a]	total
0	8.56	N/A	17.50
5	7.39	4.92E-02	15.12
10	0.18	3.10E-04	0.38
15	0.02	5.74E-05	0.05
20	0.01	4.06E-05	0.03

[a] Film permeability was decoupled from the substrate using a previously described method.[145]

4.3.3 Flame Resistance Imparted to Polyurethane Foam

In addition to high oxygen barrier, the CNF/VMT films exhibit excellent fire resistance. 2 and 4 BL of CNF/VMT coatings were deposited on a polyurethane (PU) foam and the weight gain after deposition was measured (Table IV-2). Photographs of PU foam show completely conformal coatings (Figure IV-4a). The flammability of the uncoated and coated foam was tested by holding a butane torch on one side of the foam for 10s. The uncoated foam immediately melts and drips, in agreement with previously published results.[161] No melt dripping was observed for the coated foam and the flame only traveled over the surface of the samples. The post-fire residues were imaged using SEM. As can be seen in Figure IV-4b, with just a 2 BL CNF/VMT coating, the polyurethane foam retains its original shape and cellular structure. The foam beneath the char is completely undamaged. Under higher magnification, even where the foam itself was consumed by the flame, the charred CNF/VMT film keeps its original structure, which

prevents collapse during burning. The 4 BL CNF/VMT coating exhibits even better flame resistance, with a thinner of char formed and lower weight loss. This can be ascribed to the higher coating mass than the 2 BL CNF/VMT coating (Table IV-2). The improved fire resistance is attributed to high clay loading and the nanobrick wall structure of the coating, which acts as a thermal barrier. Additionally, the improved adhesion between the CNF and VMT, as a result of LbL structuring, which induces intimate contact and strong interactions between the film components, can also improve the thermal stability of these nanocomposites.[162]

Table IV-2. Torch test results for coated and uncoated polyurethane foam.

Sample	weight gain after depositing (%)	mass loss after torch test (%)
Uncoated	-	100
2 BL CNF/VMT	3.1	31
4 BL CNF/VMT	4.4	26
2 BL Chitosan/VMT	4.1	41
4 BL Chitosan/VMT	4.8	31

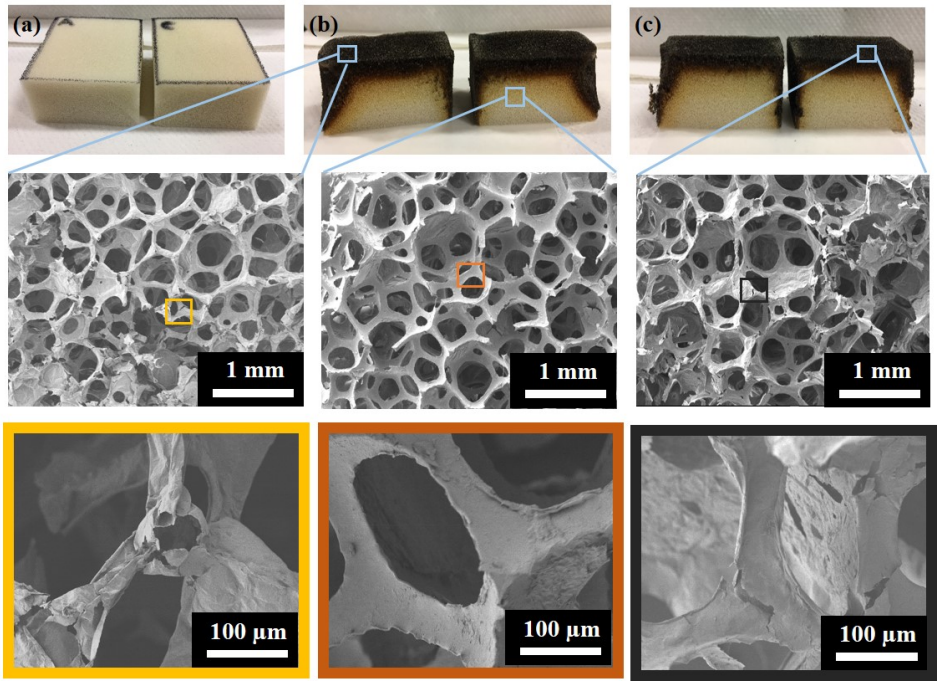

Figure IV-4. Photographs of (a) foam coated with 2 and 4 BL CNF/VMT (left and right foam, respectively) before burning. Photographs and SEM images of cross sections of PU foam coated with (b) 2 and (c) 4 BL CNF/VMT after torch testing. Boxes of the same color represent the same spot with different magnifications.

Two and four bilayer chitosan (CH)/VMT coatings were also evaluated as a comparative control to the CNF/VMT nanocoatings. Although CH/VMT coatings result in higher weight gain with the same number of bilayers deposited (Table IV-2), CNF/VMT coatings exhibit better flame protection, which can also be observed using thermogravimetric analysis. Figure IV-5 shows weight loss as a function of temperature of uncoated foam and the foam coated with 2 BL of CH/VMT or CNF/VMT. Under nitrogen atmosphere, the polyurethane foam undergoes two stages of thermal degradation, related to polyurethane hard segment depolymerization and polyol degradation.[163] Although the coated samples do not delay the onset degradation temperature, the coatings

clearly preserve the foam during thermal degradation. Uncoated foam exhibits char residue that is less than 10 wt% of its initial mass, while the residue increases to 15 wt% with the addition of the 2 BL CNF/VMT coating. The coating is only 3.1 wt% of the total mass. The 2 BL CH/VMT coating yields a char that is 13.2 wt%, despite comprising 4.1wt% of the sample. These data suggest that the cellulose-based coating imparts better heat resistance to polyurethane foam than the chitosan-based coating.

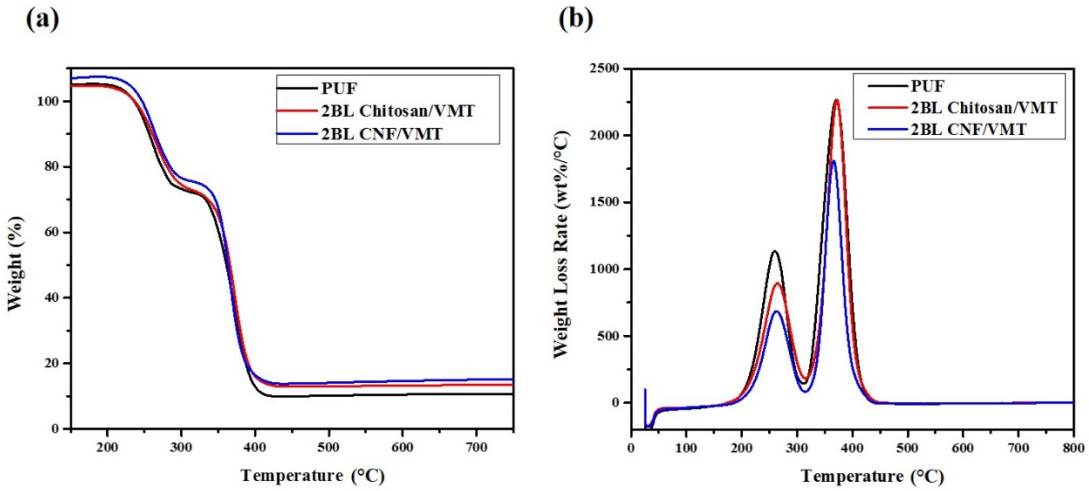

Figure IV-5. (a) Weight and (b) first derivative weight loss as a function of temperature for uncoated and LbL-coated PU foam.

4.3.4 Mechanical Properties of Thin Films

Cellulose nanofibrils generally have good mechanical properties due to their high crystallinity.[152] Incorporating clay further improves the mechanical behavior of CNF-based materials.[152] The 50 BL CNF/VMT multilayer film has an elastic modulus (E) and hardness (H) of 20 GPa and 1 GPa, respectively, which is significantly higher than other cellulose-clay composites.[152-153, 164] These improved properties can be ascribed to strong

ionic interaction between cationic CNF and anionic VMT that creates a strong interface, which improves the stress transfer.[157] The highly aligned clay platelets also contribute to the high modulus and hardness.[165] Additionally, it is believed that the fibrous CNF matrix, with large aspect ratio, strengthens the film.[142, 152]

4.4 Conclusions

Vermiculite clay platelets were assembled with cellulose nanofibrils using layer-by-layer assembly. The nanobrick wall structure, with high clay loading and orientation, results in high transparency, super gas barrier properties, excellent flame resistance, and high modulus. An oxygen permeability of 4.06×10^{-21} cm^3 cm/(cm^2 s Pa) was achieved with a 20 BL CNF/VMT coating, which is comparable to that reported for SiO_x barrier thin films commonly deposited on plastic films.[166] Only the outermost layer of flammable foam was charred during torch testing when coated with a 2 BL CNF/VMT coating (and no melt dripping occurred). An elastic modulus of 20 GPa was observed for a 50 BL CNF/VMT film, which is higher than other CNF-clay composites reported in the literature.[152-153, 164] These assembled CNF/VMT coatings offer an environmentally-benign and low-cost opportunity for various packaging and protection applications.

CHAPTER V

ULTRATHIN TRANSPARENT NANOBRICK WALL ANTICORROSION COATINGS*

5.1 Introduction

Waterborne polyurethane (PU) is widely used in coatings and adhesives due to its tailorable properties, nontoxicity, and environmental-friendliness.[115] When used by itself, polyurethane exhibits relatively high permeability to corrosive species (oxygen, water and aggressive ions), as well as poor thermal stability and mechanical strength. These disadvantages limit the use of PU as anti-corrosion coatings. Since layer-by-layer assembled polymer-clay coatings have demonstrated tremendous barrier improvement relative to all-polymer coatings, [3, 142] cationic waterborne polyurethane and anionic vermiculite clay (VMT) nanocoating were prepared. The anticorrosion performance of PU/VMT coatings was studied on aluminum (AA7075-T651) and compared with more hydrophilic PEI/VMT coatings with similar thickness to understand the influence of hydrophobicity of polyelectrolytes on corrosion protection. A 300 nm thick PU/VMT coating, provides two orders of magnitude improvement in impedance magnitude and imparts corrosion protection for five days, which is comparable to composite coatings that are two orders of magnitude thicker (and some chromate conversion coatings).[167-170] No

*Reprinted with permission from Qin, S.; Cubides, Y.; Lazar, S.; Ly, R.; Song, Y.; Gerringer, J.; Castaneda, H.; Grunlan, J. C. Ultrathin Transparent Nanobrick Wall Anticorrosion Coatings. *ACS Applied Nano Materials* **2018**, 1, 5516-5523. Copyright 2018 American Chemical Society.

surface treatments (e.g., etching and polishing) are required prior to coating due to the very good adhesion of the polyelectrolytes to aluminum.[171] It has been suggested that films consisting of polyelectrolytes provide not only barrier to aggressive species, but also the ability to buffer pH through physico-chemical reactions, which contributes to the anticorrosion behavior of these coatings.[172] Environmental-friendliness, ease of production and excellent corrosion resistance make these LbL-assembled PU/VMT coatings a potential replacement for undesirable chromate conversion coatings.

5.2 Experimental

Branched polyethylenimine (PEI) (Mw = 25,000 g/mol) was purchased from Sigma-Aldrich (Milwaukee, WI). The cationic polyurethane dispersion was donated from Lubrizol (SCR20072, Wickliffe, OH). Vermiculite clay (VMT) (Microlite 963^{++}) was purchased from Specialty Vermiculite Corp (Cambridge, MA). All chemicals were used as received. Deionized water with a specific resistance greater than 18 MΩ was used in all solutions and rinses. Films were coated on AA7075-T651 aluminum panels (~1 mm thick) obtained from Aerotech Alloys (Temecula, CA). Single side-polished silicon wafers (University Wafer, South Boston, MA) were used to measure the film thickness using profilometry.

Layer-by-layer deposition was carried out with a home-built robotic dipping system.[131] Each aluminum substrate was immersed in the PEI or PU solution for 5 min, followed by rinsing with DI water and drying with filtered air for 30 seconds, and then dipped into an anionic VMT solution for another 5 min, followed again by rinsing and

drying to complete the initial bilayer. The rest of dipping cycles used 1 min immersion times for both solutions, with the same rinsing and drying procedure in between. Multilayer assemblies are denoted as $(PEI/VMT)_x$ or $(PU/VMT)_x$, where x is the number of bilayers deposited.

A P-6 profilometer (KLA-Tencor, Milpitas, CA) was utilized to measure thin film thickness on silicon wafers. An a-SE ellipsometer (J.A Woollam Co., Inc., Lincoln, NE) was used to measure swelling ratio of the coatings in water. Visible light transmittance, between 350 and 780 nm, was measured using a USB 2000 ultraviolet−visible light (UV−vis) spectrometer (Ocean Optics, Dunedin, FL). The reported transmission was the average of transmittance between 350 and 780 nm. ^{1}H NMR spectra were obtained using solutions in deuterochloroform ($CDCl_3$) and a Varian Inova 300 MHz interfaced with a Linux based spectrometer system using VnmrJ software. Electrochemical impedance spectroscopy (EIS) was performed to evaluate the electrochemical response of the different coating samples immersed for five days in an aerated 3.5 wt% NaCl solution at room temperature. The electrochemical measurements were performed using a Gamry potentiostat/galvanostat/ZRA Reference 600TM (Warminster, PA) and a Faraday cage to prevent electromagnetic interference. EIS data were collected in a frequency range from 100 kHz to 10 mHz, with 10 points per decade, and a sinusoidal potential signal of 10 mV in regard to the open circuit potential (OCP). All electrochemical tests were performed in duplicate to ensure the reproducibility of the EIS response. Equivalent electrical circuits provided by the EC-lab V10.40 fitting software were used to fit the EIS data. Polarization experiments were carried out at room temperature in deaerated 0.1 M NaCl solutions, the

lower salt concentration was used to minimize the noise in the signal. Films were imaged using a JEOL JSM-7500F SEM (Tokyo, Japan) and a digital Keyence VH-Z100 optical microscope (Osaka, Japan). TEM samples were deposited on PET substrates and then embedded in Epofix resin (EMS, Hatfield, PA). After curing, the samples were cut with an Ultra 45° diamond knife (Diatome, Hatfield, PA). Thin sections (~100 nm thick) were collected and imaged using a Tecnai G2 F20 (FEI, Hillsboro, OR) operated at 200 kV. X-ray diffraction was performed with a Bruker-AXS D8 Advance X-ray Diffractometer (Billerica, MA) in the range of $2\theta=20^{\circ}$ to 90°.

5.3 Results and discussion

5.3.1 Multilayer Film Morphology

PEI/VMT and PU/VMT multilayer films were prepared by alternately dipping an aluminum substrate into polyelectrolyte solutions and a vermiculite clay suspension (illustrated in Figure V-1a). As shown in Figure V-1b, uniform coatings were prepared on PET and aluminum without any etching or polishing pretreatments. The visible light transparency of the PU/VMT coatings was measured as a function of bilayers deposited (Figure V-1e), which is comparable to that of PEI/VMT LbL gas barrier coatings.[173] This high transparency suggests good orientation and exfoliation of VMT platelets inside the films.[121, 174] The highly ordered clay can be observed in a cross-sectional TEM image (Figure V-1c), where individual clay platelets appear as dark lines due to their high electron density. It has been estimated that these coatings add no more than 0.05% weight to the aluminum plates.

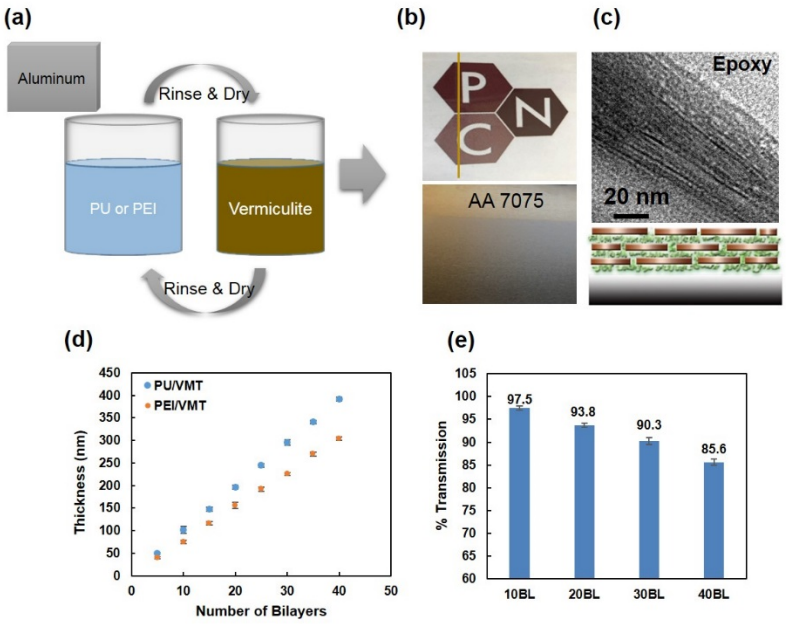

Figure V-1. (a) Schematic of the LbL assembly process. (b) Digital images of $(PU/VMT)_{10}$ coatings deposited on coated on PET (right side of yellow line), uncoated PET (left side of yellow line) and bare aluminum. (c) Cross-sectional TEM image of a $(PU/VMT)_{10}$ coating on PET and schematic of the thin film structure. (d) Growth curves for PU/VMT and PEI/VMT multilayer coatings. (e) Visible light transmittance as a function of PU/VMT bilayers deposited on quartz slides.

Growth of these polyelectrolyte/clay assemblies was monitored as a function of the number of bilayers deposited. Figure V-1d shows a linear increase in thickness with bilayer number. The growth rates were calculated to be ~8 nm and ~10 nm per bilayer for PEI/VMT and PU/VMT, respectively. The difference in growth rate is probably due to different chain conformations of PEI and PU in the multilayer films. It is likely that the polyurethane has a more coiled conformation due to a lower degree of ionization compared with PEI. As can be confirmed with ^{1}H NMR (Figure V-2a-b), polyurethane contains long aliphatic chains with few cationic amine groups, so the ratio of aliphatic region over amine moieties of PU is much lower than that of PEI. As a result, the

concentration of positively charged amine groups is much higher in PEI chains. More hydrophilic amine groups can easily bond with more water molecules and chloride ions, which leads to greater film swelling and thus the creation of more diffusion pathways. When exposed to a 3.5% NaCl solution, PEI/VMT swells to 91% of its initial thickness, while PU/VMT swells less than 40% (Figure V-2c). Moreover, the transport of aggressive ions (mostly Cl-) within the polyelectrolyte films occurs by hopping between ion-exchange sites.[175-176] For a chloride ion, each extrinsically compensated amine group is a hopping site, and a Cl^- first pairs with one site and then jumps to an adjacent site. The amine groups act as charge carriers, and fewer carriers per chain can slow the Cl^- transport and retard the corrosion (Figure V-2d).

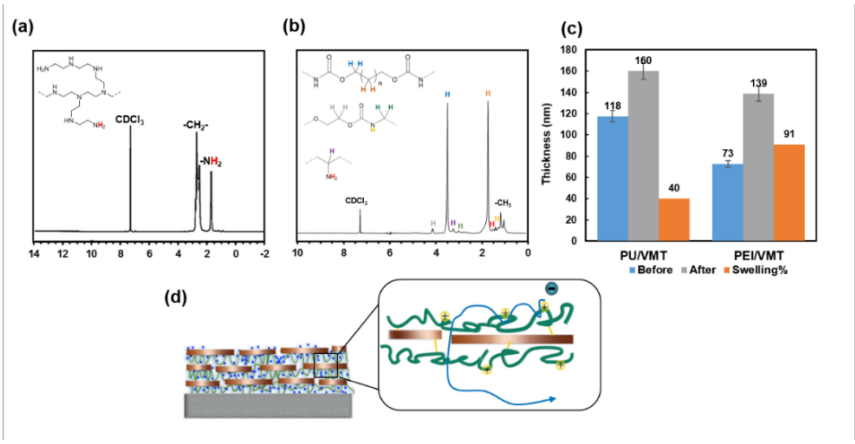

Figure V-2. NMR spectra of (a) branched polyethylenimine and (b) polyurethane. (c) The swelling ratio of (PEI/VMT)10 and (PU/VMT)10 coatings in 3.5% NaCl solution. (d) Schematic of ion transport in these LbL assembled films.

5.3.2 Anticorrosion Performance

Electrochemical impedance spectroscopy is considered one of most reliable and non-destructive electrochemical techniques for studying coating degradation mechanisms,

as well as metal/electrolyte interfacial processes.[177] It was used here to evaluate corrosion resistance of the polyelectrolyte/clay coatings. Four different thickness of LbL assembled PU/VMT coatings (i.e., 10, 20, 30, and 40BL) as well as $(PEI/VMT)_{40}$ were tested for 5 days to observe the influence of coating thickness and polymer species on corrosion of aluminum. The five-day immersion was chosen because the thin multilayer coating is being evaluated only as a pretreatment rather than a standalone anti-corrosion system. Figure V-3 shows the EIS spectra for PU/VMT coatings with varying thickness (i.e., bilayers). Two time constants were identified from the phase angle-Bode plots. The time constant at high frequency (~ 104 Hz) is associated with the coating physical characteristics (e.g., resistivity to water and ion diffusion), whereas the one at intermediate frequencies (1 to 10 Hz) is related to the passive layer (i.e., Al_2O_3) at the aluminum/coating interface. During the entire immersion time (i.e., from Day 1 to Day 5), only one EIS pattern was identified for $(PU/VMT)_{20,}$ $(PU/VMT)_{30,}$ and $(PU/VMT)_{40}$ (Figure V-3 b-d), which suggests that no corrosion process was initiated during the test period. In contrast, three different EIS patterns were observed for $(PU/VMT)_{10}$ (Figure V-3a) and $(PEI/VMT)_{40}$, which suggests three stages of degradation. For Day 1, the coatings showed similar behavior to the thicker ones, with a large capacitive loop in the Nyquist plot and the impedance magnitude at 0.01 Hz ($|Z|_{0.01Hz}$) close to 10^6 Ω cm^2. The $|Z|_{0.01Hz}$ is often used as a first approximation to evaluate the corrosion resistance of a coating because it is associated with the total corrosion resistance of the system.[178-179] A significant decrease at $|Z|_{0.01Hz}$ started on the second day of exposure and an inductive behavior at low frequency ($\sim 10^{-1}$ Hz) can be observed, which suggests the breakdown of the passive layer due to the

adsorption of chloride ions at the interface. Similar behavior was also observed with uncoated aluminum. After three days of immersion, the inductive behavior disappeared and the $|Z|_{0.01Hz}$ value increased, which can be the result of formation of solid corrosion products that block active sites on the aluminum surface and slow down the charge transfer corrosion process.

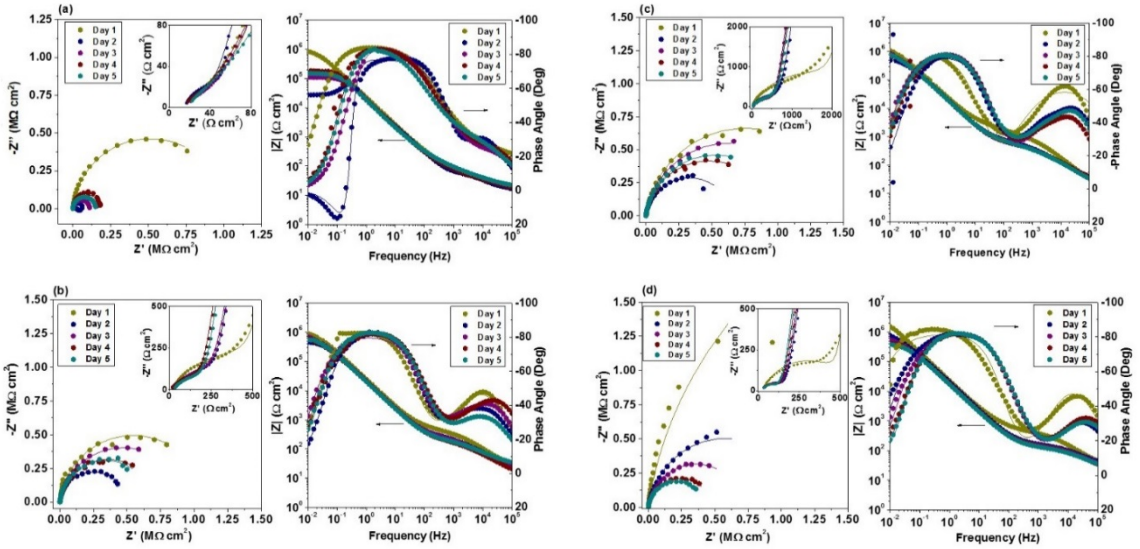

Figure V-3. EIS spectra (Nyquist and Bode plots) of (a) $(PU/VMT)_{10}$, (b) $(PU/VMT)_{20}$, (c) $(PU/VMT)_{30}$, and (d) $(PU/VMT)_{40}$ deposited on aluminum, for up to five days in 3.5 wt.% NaCl solution.

To further understand the electrochemical behavior of these coatings, equivalent electrical circuits were used to fit the EIS data. In these circuits, illustrated in Figure V-4, R_s corresponds to the resistance of the electrolyte (i.e., 3.5% NaCl). Q_{ox} and R_{ox} correspond to the capacitance and the resistance of the oxide film and corrosion products formed at the aluminum surface, and similarly, Q_c and R_c correspond to the capacitance and the resistance of the LbL deposited coatings. Q_{dl} and R_{ct} describe the double layer

capacitance and the charge transfer resistance associated with the corrosion process at the aluminum/electrolyte interface. L represents the inductance observed at low frequency.[180] In general, as water and electrolytes diffuse into the coating, Q_c increases (as a result of the increased dielectric constant) and R_c decreases.[181] For $(PU/VMT)_{10}$, three different equivalent circuits were used to describe the three different EIS patterns (Figure V-3a), with Circuit A (Figure V-4a) for Day 1, Circuit B (Figure V-4b) for Day 2, where the adsorption behavior is observed, and Circuit C (Figure V-4c) for Day 3-5. Circuit A was also used for thicker films and Circuit D was used for bare (i.e., uncoated) aluminum. For all the different equivalent circuits, constant phase elements (CPEs) were used instead of capacitances in order to account for deviations from ideal capacitive behavior coming from heterogeneities in the coating matrix, porosity, mass transport of electrolyte, and relaxation processes.[180, 182]

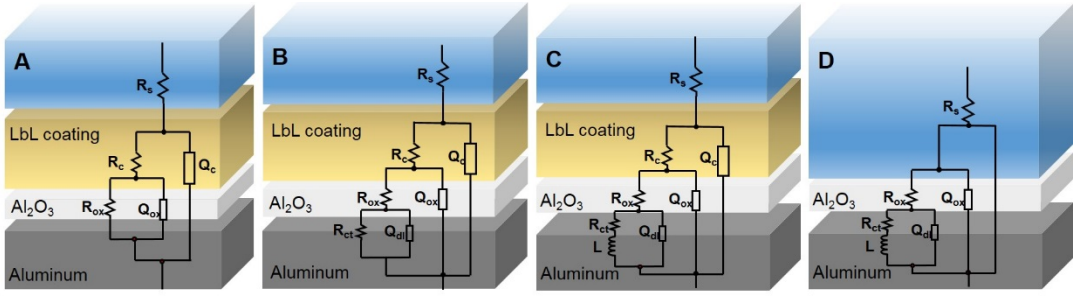

Figure V-4. Equivalent electrical circuits used to fit the EIS data for bare aluminum and the different polymer-nanoclay composite coatings immersed for five days in 3.5 wt% NaCl solution.

Based on the fitting results, selected equivalent circuit elements were plotted and the polarization resistance (R_p) was calculated, which is defined as the impedance value at 0 HZ ($Z_{\omega\to 0} = R_s + R_p \approx R_p$) that describes the total corrosion resistance of the system.[183-184] The evolution of R_p for all samples is shown in Figure V-5a. For the

$(PU/VMT)_{20,}$ $(PU/VMT)_{30}$, and $(PU/VMT)_{40}$ coatings, the R_p values were significantly higher (~10^6 Ω cm^2) compared with that of the bare metal (~10^4 Ω cm^2) and remained stable during the entire test. These high R_p values are due to high R_{ox} values (associated with the resistance of passive oxide film and corrosion products) being achieved. The good barrier provided by the coatings slows down water and electrolyte uptake, which is associated with a lower capacitance (Q_c) and a higher resistance (R_c) of the coating, and protects the passive Al_2O_3 layer from aggressive ions. Even when water and electrolytes penetrate through the film, the existence of a passive oxide layer can still provide protection against initiation of corrosion at the metal surface. It's also possible that the strong adhesion between coating and Al_2O_3, as a result of ionic and hydrogen bonding, hinders the adsorption of chloride ions at the interface.[185] Despite having similar R_p for the first day, a dramatic decrease in $(PU/VMT)_{10}$ and $(PEI/VMT)_{40}$ films was observed during the following days. As mentioned before, this is related to the breakdown of the passive layer due to the charge transfer process triggered by chloride adsorption, and the subsequent increase of R_p is probably due to the formation of corrosion products.

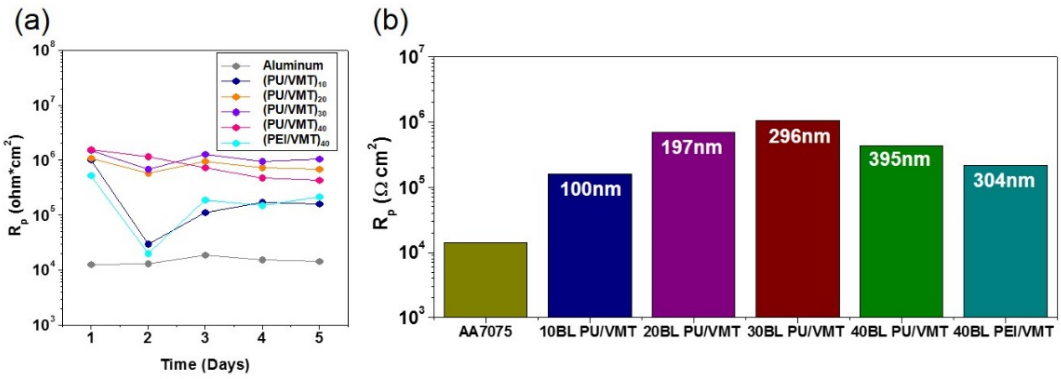

Figure V-5. (a) R_p evolution for samples immersed for 5 days in a 3.5 wt.% NaCl solution. (b) Rp values of all samples on Day 5.

Figure V-5b summarizes the R_p values for all samples after a 5-day immersion. For PU/VMT films, the R_p first increases with coating thickness and then decreases. The initial increase is due to thicker coatings providing better barrier due to a greater tortuous diffusion pathway and higher coating mass. However, more dipping cycles are required to assemble thicker films, which means longer exposure of the aluminum substrate to aqueous solutions that could initiate corrosion, leading to a lower R_p of $(PU/VMT)_{40}$. This is confirmed by the observation of $Al(OH)_3$ as a corrosion product, which typically forms around the precipitates such as $MgZn_2$, AlCu, and Mg in aluminum alloys,[84] on all LbL coated samples. Although $(PU/VMT)_{30}$ has similar thickness with $(PEI/VMT)_{40}$, it exhibits almost six times higher polarization resistance. As discussed before, the high efficiency of PU coatings is probably a result of hydrophobicity and the lower degree of ionization due to fewer positively-charged amine groups, which leads to better barrier (higher R_c and lower Q_c). This hydrophobicity, when combined with highly aligned VMT platelets, leads to a dramatic improvement in the corrosion resistance. A 300 nm $(PU/VMT)_{30}$ coating exhibits significant anticorrosion performance, with two orders of magnitude higher polarization resistance compared with the bare metal, even after 5 days. The better performance of these polyurethane coatings is also in agreement with the results from polarization experiments amongst bare aluminum, $(PU/VMT)_{30}$ and $(PEI/VMT)_{40}$, where $(PU/VMT)_{30}$ showed the lowest anodic current density. Optical images of the three samples after polarization also confirms better protection from $(PU/VMT)_{30}$.

Figure V-6 shows the SEM and optical images of bare aluminum, $(PU/VMT)_{30}$ and $(PEI/VMT)_{40}$ coatings before and after 5-day EIS testing. Homogenous LbL protective

coatings can be observed, having been deposited without any surface treatment (Figure V-6b-c). Even with a lower impedance magnitude, $(PEI/VMT)_{40}$ still shows some corrosion protection. Both coatings maintained their surface morphologies after the 5-day exposure, which indicates no or very few corrosion products were formed (the pressure from corrosion products formation can cause cracking and even delamination of a coating).[186] No significant morphology change or coating delamination was observed, even following a 15-day immersion, suggesting good coating stability and adhesion. However, the bare aluminum corroded and corrosion products were formed on the surface after 5 days. Those corrosion products grew into a thick porous layer after the 15-day exposure. Owing to the high transparency of the LbL deposited coatings, the corrosion in the coating/substrate interface can be directly monitored with an optical microscope. As can be seen in Figure V-6d, the uncoated aluminum sample corroded severely, showing large pits and a layer of corrosion products, while there is no significant evidence of corrosion products on the interface for the coated samples.

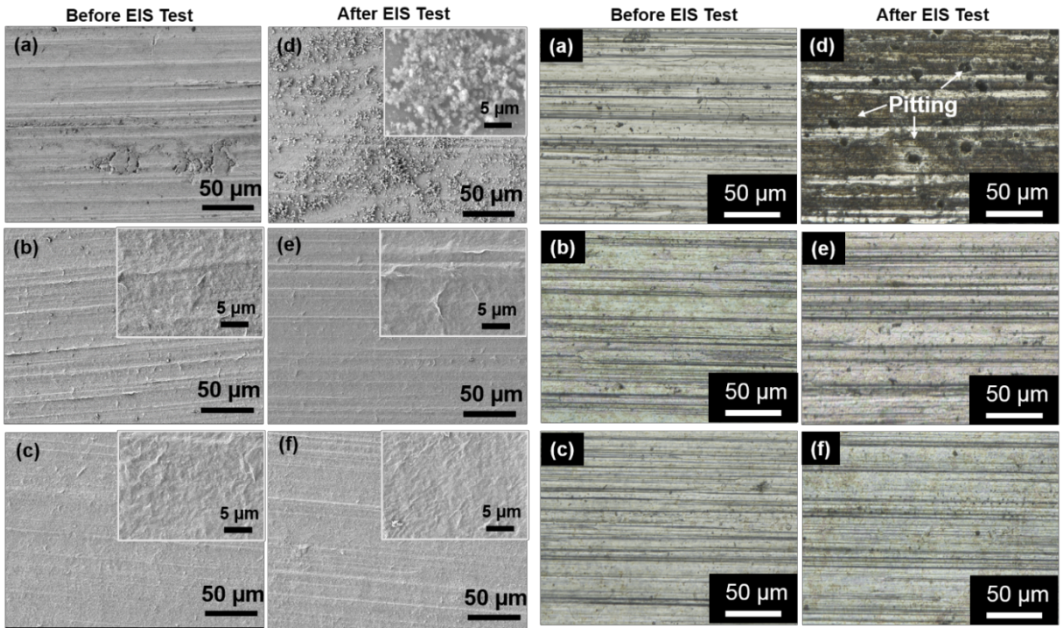

Figure V-6. SEM (left two columns) and optical microscope (right two columns) images of (a) uncoated aluminum, (b) $(PEI/VMT)_{40}$, and (c) $(PU/VMT)_{30}$ before the EIS test, along with (d) uncoated aluminum, (e) $(PEI/VMT)_{40}$, and (f) $(PU/VMT)_{30}$ after a 5-day immersion in a 3.5% NaCl solution.

5.4 Conclusions

A simple and very effective treatment method for corrosion protection is developed here. Ionically assembled films prepared with cationic polyurethane and anionic clay, are used for the first time to provide corrosion protection for aluminum. A $(PU/VMT)_{30}$ coating, with the thickness of only 300 nm, improves the impedance of aluminum by two orders of magnitude. Moreover, this thin coating can maintain the corrosion protection for at least 5 days, which is a long time considering the small thickness. This effective anticorrosion performance is due to high barrier imparted by the nanobrick wall morphology and the ability to maintain this barrier in an aqueous environment due to the lower degree of ionization of PU. Future work could include

depositing a complete multilayer corrosion coating, with the PU/VMT coating as a pretreatment, and performing salt spray test ASTM B117 to evaluate the real world corrosion protection. In short, the present study provides a new concept for a highly effective, transparent and environmentally-friendly anticorrosion layer that could potentially be used as a pretreatment for aluminum alloys.

CHAPTER VI

CONCLUSIONS AND FUTURE WORK

6.1 New and Improved Functionality Developments for Polyelectrolyte-Clay Assemblies

This dissertation described varying functionalities of LbL-assembled films and provided a better understanding of structure-property relationships. By incorporating highly aligned clay into a hydrogen-bonded polymer matrix, a stretchable gas barrier system was shown to overcome the stretchability-permeability trade-off, exhibiting the best barrier at high strain. A similar strategy was applied to cellulose-based coatings to improve the barrier and flame resistance of this biodegradable polymer. The polymer-clay structure has also shown great potential in corrosion protection.

6.1.1 Combined High Stretchability and Gas Barrier in Hydrogen-Bonded Multilayer Nanobrick Wall Thin Films

It was shown in Chapter III that a stretchable gas barrier was developed on polyurethane substrate with the combination of both high stretchability and barrier performance. Highly aligned clay platelets were incorporated into a hydrogen bonded polymeric matrix with LbL assembly. This stretchable gas barrier coating rivals most organic or inorganic coatings, achieving the highest barrier reported at high strain. A 10 BL PEO/PAA+MMT film (432 nm thick) remained 46X OTR reduction at 20% strain, with five orders of magnitude lower permeability than that of polyurethane rubber

substrate. This coating system, with high barrier at high strain, provides a new strategy of making high performance stretchable gas barrier for elastomeric substrates.

6.1.2 Super Gas Barrier and Fire Resistance of Nanoplatelet/Nanofibril Multilayer Thin Films

Chapter IV described a method to improve the flame resistance and gas barrier properties of cellulose-based films with highly aligned vermiculite clay (VMT) using the layer-by-layer deposition process. A 136 nm (20 BL) CNF/VMT coating shows an OTR of 0.013 cc/(m^2 day atm). A 2 BL of CNF/VMT coating prevents flexible polyurethane (PU) foam from melting when exposed to a butane torch. These nanocoatings also exhibit a high elastic modulus (20 GPa) and hardness (1 GPa). This study demonstrates a unique, renewable, and cellulose-based nanocoating that could be used in a variety of packaging and protection applications.

6.1.3 Ultrathin Transparent Nanobrick Wall Anticorrosion Coatings

High corrosion resistance was demonstrated with LbL assembled polyurethane (PU) and vermiculite (VMT) clay multilayer films in Chapter V. The combination of relatively hydrophobic polyurethane and highly aligned clay platelets leads to excellent barrier properties. A 30 bilayer PU/VMT coatings (300 nm thick) provides two orders of magnitude higher impedance and imparts corrosion protection for five days, which could be a potential environmentally friendly replacement for chromate conversion coatings (CCCs).

6.2 Future Directions

6.2.1. Improving Moisture Barrier of SiO_x with Polyelectrolyte Layers

In addition to good gas barrier, moisture barrier is also critical for packaging and electronics.[187-188] Electronic devices such as liquid crystal displays (LCDs), organic photovoltaic cell (OPVs), and organic light-emitting diodes (OLEDs) require a very low water vapor transmission rate (WVTR) (e.g., less than 10^{-6} g/m^2 day for OLEDs).[6, 72, 189] Despite exhibiting outstanding oxygen barrier,[190] PEM coatings alone exhibit very limited moisture barrier as a result of loosened chain packing and higher chain mobility in humid conditions.[191-192] SiO_x thin films can exhibit good moisture barrier but rigidity that leads to cracking is a challenge for flexible packaging.

Here we report a new multilayer moisture barrier system that combines a thin PVD-prepared SiO_x layer sandwiched between LbL-assembled PEM layers. An 8 bilayer (BL) polyethylenimine (PEI)/ poly acrylic acid (PAA) coating is used here as the PEM layer due to its high oxygen barrier and relatively high modulus.[190] The influence of each layer is investigated by comparing the barrier performance of single- or two-layer films based on SiO_x and PEM. When applying a single PEM layer above or below the with a SiO_x layer (i.e., a two –layer system), the moisture barrier was small. The barrier of the three-layer system (PEM/SiO_x/PEM) was improved by a factor of 8 relative to PET substrate. This appears to be the best moisture barrier achieved among PEM-based systems to-date, highlighting the great synergy between these layers and the tremendous potential of making metal oxide ultrabarriers using PEM layers.

Multilayer thin films were prepared with the combination of layer-by-layer assembly (LbL) and physical vapor deposition (PVD) techniques. As shown in Figure VI-1, an 8 BL PEI/PAA coating (~800 nm) was first deposited on the PET substrate, followed by a 20 nm SiO_x layer and another 8 BL PEI/PAA layer. Besides the three-layer film (PEM+SiO_x+PEM), single-or double-layer thin films based on SiO_x and PEM were also prepared in order to understand the optimized structure. All samples are homogeneous and highly transparent, with the visible light transmittance above 94% (Figure VI-2). This high transparency suggests refractive index matching between from SiO_x and PEM. Differing refractive indices between each adjacent layer will cause light scattering and absorption, which diminish the transmission of visible light.[193-194]

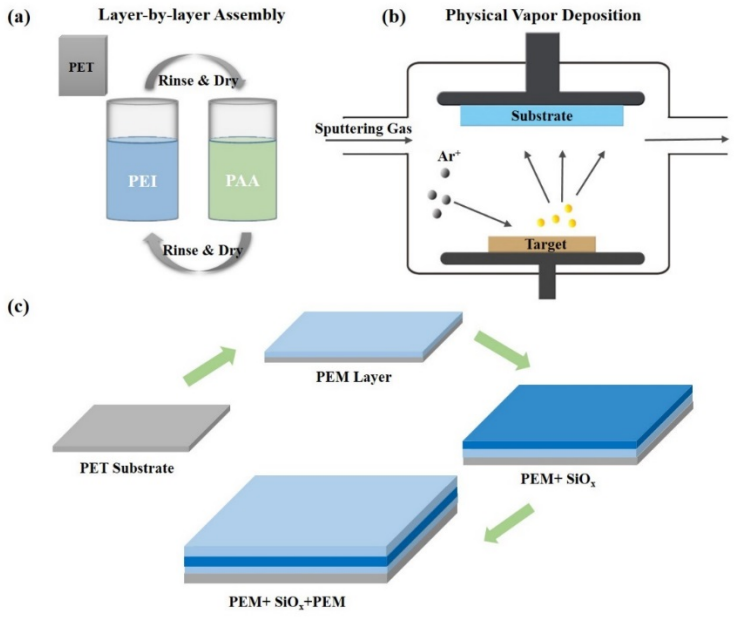

Figure VI-1. Schematic representation of (a) layer-by-layer assembly of PEM (e.g. PEI/PAA) coatings, (b) physical vapor deposition of SiO_x layers, (c) multilayer thin film preparation with PEM and SiO_x layers.

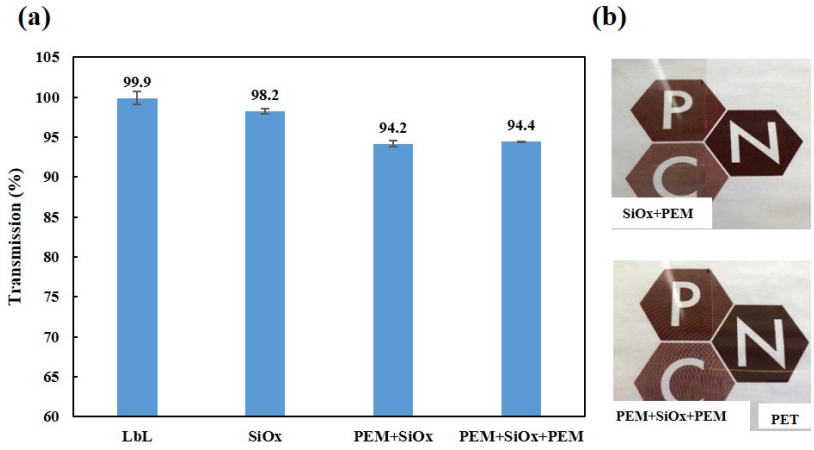

Figure VI-2. (a) Visible light transmission of multilayer thin films based on SiOx and PEM layers. (b) Digital photographs of SiOx+PEM and PEM+SiOx+PEM coated on PET substrate.

Figure VI-3 shows the water vapor transmission rate (WVTR) of various samples deposited on 179 um PET substrates. Single PEM and SiO_x layers exhibit high WVTR values of 2.74 and 2.38 g/m^2 day, respectively. For the 16-bilayer PEM layer, it swells significantly in high humidity, which opens up more diffusion pathways.[191] The WVTR for SiO_x is similar to previous literature reports.[195] SiO_x has a much lower permeability ($1.53*10^{-4}$ g mm/m^2 day atm) than PEM ($1.53*10^{-4}$ g mm/m^2 day atm) due to its relatively small thickness. Even so, its barrier performance is limited by defects.

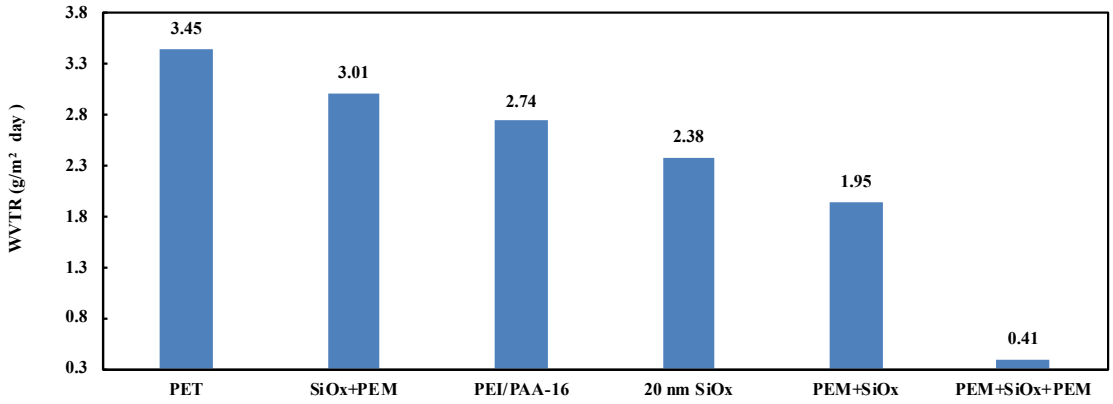

Figure VI-3. Water vapor transmission rate (WVTR) of various samples coated on 179 μm PET substrate, measurements were conducted at 38°C 90% RH.

Applying a PEM layer underneath the SiO_X (i.e., PEM+SiO_x) decreases the WVTR decreased from 2.38 to 1.95 g/m^2 day. This improved barrier is correlated with the changed surface morphology of SiO_x layer. It is well known that a smooth surface is needed to reduce the shadow effect that results in coating non-uniformity. After being exposed to humid conditions, the underlying PEI/PAA layer experiences increased polymer chain mobility that creates a smooth surface, with roughness around 1.2 nm.[190] Additionally, PEI has been widely used as an adhesive due to its reactive amine groups.[196] More importantly, the high modulus of PEI/PAA decreases the stiffness mismatch between the substrate and the SiO_X layer. It has been reported that the modulus for uncoated PET is about 3 GPa,[129] while SiO_X is around 60 GPa.[197] This mismatch can cause large residual compressive stresses that can cause cracking and delamination.

Applying another PEM layer atop SiO_x imparts further barrier improvement. As shown in Figure VI-3, the three-layer "sandwich" coating, exhibits a WVTR of 0.41 g/m^2

day, which improves the moisture barrier of PET by nearly an order of magnitude. Laminate theory would predict a WVTR of 2.09 g/m^2 day. The much lower experimental value suggests there is a synergistic benefit with this multilayer structure, where the first glassy PEM layer creates a denser and more uniform SiO_x and the second PEM layer fills any remaining defects. The elimination of the defects with a PEM top layer will be further examined with scanning electron microscopy and atomic force microscopy. We expect to see better moisture barrier improvement with more organic-inorganic layer pairs, and barrier can be further improved by exploiting different PEM systems.

6.2.2 Corrosion Protection Coatings with PEM Barrier Coating and Hydrophobic Surface

As demonstrated in Chapter V, assembling cationic polyurethane with anionic vermiculite clay produces coatings with excellent corrosion resistance due to high tortuosity and overall hydrophobicity. Even so, as water molecules diffuse inside, the coating swells and opens up more diffusion pathway for corrosive species, which deteriorates the barrier performance. Therefore, applying a water-repellent topcoat could be an effective way to improve the corrosion protection of LbL barrier coatings. For example, a superhydrophobic poly(perfluorodecyl acrylate-*co*-ethylene glycol diacrylate) (P(PFDA-*co*-EGDA)) top layer on polyethylene glycol diacrylate (PEGDA) bottom layer reduced the corrosion rate of copper by four orders of magnitude.[198]

Recently, a superhydrophobic surface was prepared with layer-by-layer assembly of Nafion and polyethylenemine (PEI).[199] Contact angle as high as 160° was observed with only 3 BL due to the microporous structure and the fluorinated surface.[199] Improved

corrosion protection is expected from PU/VMT coatings with PEI/Nafion as a topcoat. Additionally, inspired by the *Nepenthes* pitcher plant, researchers have developed slippery liquid-infused porous surfaces (SLIPS) that utilize microporosity to anchor a thin layer of lubricant.[200] The existence of lubricant layer provides great robustness and enables excellent properties such as omniphobicity,[201] anti-icing,[202] and anti-fouling.[203] The LbL assembled PEI/Nafion has also demonstrated the ability to form a SLIPS system after being infused with lubricants,[199] which could further improve the durability of the hydrophobic coating proposed here.

REFERENCES

1. Dou, Y.; Pan, T.; Xu, S.; Yan, H.; Han, J.; Wei, M.; Evans, D. G.; Duan, X., Transparent, ultrahigh-gas-barrier films with a brick–mortar–sand structure. *Angewandte Chemie International Edition* **2015,** *54,* 9673.

2. Robertson, G. L., *Food packaging: Principles and practice*. CRC press: 2016.

3. Priolo, M. A.; Holder, K. M.; Guin, T.; Grunlan, J. C., Recent advances in gas barrier thin films via layer-by-layer assembly of polymers and platelets. *Macromolecular Rapid Communications* **2015,** *36,* 866.

4. Affinito, J.; Gross, M.; Coronado, C.; Graff, G.; Greenwell, I.; Martin, P., A new method for fabricating transparent barrier layers. *Thin Solid Films* **1996,** *290,* 63.

5. Inagaki, N.; Tasaka, S.; Nakajima, T., Preparation of oxygen gas barrier polypropylene films by deposition of siox films plasma-polymerized from mixture of tetramethoxysilane and oxygen. *Journal of Applied Polymer Science* **2000,** *78,* 2389.

6. Burrows, P. E.; Graff, G. L.; Gross, M. E.; Martin, P. M.; Shi, M.-K.; Hall, M.; Mast, E.; Bonham, C.; Bennett, W.; Sullivan, M. B., Ultra barrier flexible substrates for flat panel displays. *Displays* **2001,** *22,* 65.

7. Renner, F.; Stierle, A.; Dosch, H.; Kolb, D.; Lee, T.-L.; Zegenhagen, J., Initial corrosion observed on the atomic scale. *Nature* **2006,** *439,* 707.

8. Shchukin, D. G.; Zheludkevich, M.; Yasakau, K.; Lamaka, S.; Ferreira, M. G.; Möhwald, H., Layer-by-layer assembled nanocontainers for self-healing corrosion protection. *Advanced Materials* **2006,** *18,* 1672.

9. Richardson, J. J.; Cui, J.; Bjornmalm, M.; Braunger, J. A.; Ejima, H.; Caruso, F., Innovation in layer-by-layer assembly. *Chemical Reviews* **2016,** *116,* 14828.

10. Xiao, F.-X.; Pagliaro, M.; Xu, Y.-J.; Liu, B., Layer-by-layer assembly of versatile nanoarchitectures with diverse dimensionality: A new perspective for rational construction of multilayer assemblies. *Chemical Society Reviews* **2016,** *45,* 3088.

11. Kharlampieva, E.; Kozlovskaya, V.; Sukhishvili, S. A., Layer-by-layer hydrogen-bonded polymer films: From fundamentals to applications. *Advanced Materials* **2009,** *21,* 3053.

12. Tian, Y.; He, Q.; Tao, C.; Li, J., Fabrication of fluorescent nanotubes based on layer-by-layer assembly via covalent bond. *Langmuir* **2006,** *22,* 360.

13. Kotov, N., Layer-by-layer self-assembly: The contribution of hydrophobic interactions. *Nanostructured Materials* **1999,** *12,* 789.

14. Ye, S.; Wang, C.; Liu, X.; Tong, Z., Deposition temperature effect on release rate of indomethacin microcrystals from microcapsules of layer-by-layer assembled chitosan and alginate multilayer films. *Journal of Controlled Release* **2005,** *106,* 319.

15. Priolo, M. A.; Gamboa, D.; Grunlan, J. C., Transparent clay− polymer nano brick wall assemblies with tailorable oxygen barrier. *ACS Applied Materials & Interfaces* **2009,** *2,* 312.

16. Dubas, S. T.; Schlenoff, J. B., Swelling and smoothing of polyelectrolyte multilayers by salt. *Langmuir* **2001,** *17,* 7725.

17. Priolo, M. A.; Holder, K. M.; Gamboa, D.; Grunlan, J. C., Influence of clay concentration on the gas barrier of clay–polymer nanobrick wall thin film assemblies. *Langmuir* **2011,** *27,* 12106.

18. Song, Y.; Lugo, E. L.; Powell, S.; Tzeng, P.; Wilhite, B. A.; Grunlan, J. C., Highly selective multilayer polymer thin films for co2/n2 separation. *Journal of Polymer Science Part B: Polymer Physics* **2017,** *55,* 1730.

19. Qin, S.; Song, Y.; Floto, M. E.; Grunlan, J. C., Combined high stretchability and gas barrier in hydrogen-bonded multilayer nanobrick wall thin films. *ACS Applied Materials & Interfaces* **2017,** *9,* 7903.

20. Holder, K. M.; Smith, R. J.; Grunlan, J. C., A review of flame retardant nanocoatings prepared using layer-by-layer assembly of polyelectrolytes. *Journal of Materials Science* **2017,** *52,* 12923.

21. Ariga, K.; Lvov, Y. M.; Kawakami, K.; Ji, Q.; Hill, J. P., Layer-by-layer self-assembled shells for drug delivery. *Advanced drug delivery reviews* **2011,** *63,* 762.

22. Kharlampieva, E.; Kozlovskaya, V.; Tyutina, J.; Sukhishvili, S. A., Hydrogen-bonded multilayers of thermoresponsive polymers. *Macromolecules* **2005,** *38,* 10523.

23. Yost, A. L.; Shahsavari, S.; Bradwell, G. M.; Polak, R.; Fachin, F.; Cohen, R. E.; McKinley, G. H.; Toner, M.; Rubner, M. F.; Wardle, B. L., Layer-by-layer functionalized nanotube arrays: A versatile microfluidic platform for biodetection. *Microsystems & Nanoengineering* **2015,** *1,* 15037.

24. Gu, Y.; Zacharia, N. S., Self-healing actuating adhesive based on polyelectrolyte multilayers. *Advanced Functional Materials* **2015,** *25,* 3785.

25. Pappa, A.-M.; Inal, S.; Roy, K.; Zhang, Y.; Pitsalidis, C.; Hama, A.; Pas, J.; Malliaras, G. G.; Owens, R. M., Polyelectrolyte layer-by-layer assembly on organic electrochemical transistors. *ACS Applied Materials & Interfaces* **2017,** *9,* 10427.

26. Blackburn, J. L.; Ferguson, A. J.; Cho, C.; Grunlan, J. C., Carbon-nanotube-based thermoelectric materials and devices. *Advanced Materials* **2018,** *30,* 1704386.

27. Siracusa, V.; Rocculi, P.; Romani, S.; Dalla Rosa, M., Biodegradable polymers for food packaging: A review. *Trends in Food Science & Technology* **2008,** *19,* 634.

28. Cui, Y.; Kumar, S.; Kona, B. R.; van Houcke, D., Gas barrier properties of polymer/clay nanocomposites. *Rsc Advances* **2015,** *5,* 63669.

29. Freeman, B. D., Basis of permeability/selectivity tradeoff relations in polymeric gas separation membranes. *Macromolecules* **1999,** *32,* 375.

30. Lee, W., Selection of barrier materials from molecular structure. *Polymer Engineering & Science* **1980,** *20,* 65.

31. Choudalakis, G.; Gotsis, A. D., Permeability of polymer/clay nanocomposites: A review. *European Polymer Journal* **2009,** *45,* 967.

32. Barrer, R.; Rideal, E. K., Activated diffusion in membranes. *Transactions of the Faraday Society* **1939,** *35,* 644.

33. Van Krevelen, D. W.; Te Nijenhuis, K., *Properties of polymers: Their correlation with chemical structure; their numerical estimation and prediction from additive group contributions*. Elsevier: 2009.

34. Nelson, R., Society for research of polymerized compound surfaces. *Fukui City, July* **1993,** *9*.

35. Elrawemi, M.; Blunt, L.; Fleming, L.; Bird, D.; Robbins, D.; Sweeney, F., Modelling water vapour permeability through atomic layer deposition coated photovoltaic barrier defects. *Thin Solid Films* **2014,** *570,* 101.

36. Greener, J.; Pearson, G.; Cakmak, M., *Roll-to-roll manufacturing: Process elements and recent advances*. John Wiley & Sons: 2018.

37. Siracusa, V.; Rocculi, P.; Romani, S.; Rosa, M. D., Biodegradable polymers for food packaging: A review. *Trends in Food Science & Technology.* **2008,** *19,* 634.

38. Worm, B.; Lotze, H. K.; Jubinville, I.; Wilcox, C.; Jambeck, J., Plastic as a persistent marine pollutant. *Annual Review of Environment and Resources* **2017,** *42*.

39. Tharanathan, R., Biodegradable films and composite coatings: Past, present and future. *Trends in Food Science & Technology* **2003,** *14,* 71.

40. Auras, R. A.; Singh, S. P.; Singh, J. J., Evaluation of oriented poly (lactide) polymers vs. Existing pet and oriented ps for fresh food service containers. *Packaging Technology and Science: An International Journal* **2005,** *18,* 207.

41. Cabedo, L.; Luis Feijoo, J.; Pilar Villanueva, M.; Lagarón, J. M.; Giménez, E. In *Optimization of biodegradable nanocomposites based on apla/pcl blends for food packaging applications*, Macromolecular Symposia, Wiley Online Library: 2006; pp 191.

42. De Baets, S.; Vandamme, E.; Steinbuchel, A., *Polysaccharides ii: Polysaccharides of eukaryotes*. Chemical Industry Press: 2004.

43. Siqueira, G.; Bras, J.; Dufresne, A., Cellulosic bionanocomposites: A review of preparation, properties and applications. *Polymers* **2010,** *2,* 728.

44. Klemm, D.; Kramer, F.; Moritz, S.; Lindström, T.; Ankerfors, M.; Gray, D.; Dorris, A., Nanocelluloses: A new family of nature-based materials. *Angewandte Chemie International Edition* **2011,** *50,* 5438.

45. Eichhorn, S. J.; Dufresne, A.; Aranguren, M.; Marcovich, N.; Capadona, J.; Rowan, S.; Weder, C.; Thielemans, W.; Roman, M.; Renneckar, S., Current international research into cellulose nanofibres and nanocomposites. *Journal of Materials Science* **2010,** *45,* 1.

46. Kontturi, E.; Laaksonen, P.; Linder, M. B.; Gröschel, A. H.; Rojas, O. J.; Ikkala, O., Advanced materials through assembly of nanocelluloses. *Advanced Materials* **2018,** 1703779.

47. Nechyporchuk, O.; Belgacem, M. N.; Bras, J., Production of cellulose nanofibrils: A review of recent advances. *Industrial Crops and Products* **2016,** *93,* 2.

48. Postek, M. T.; Vladár, A.; Dagata, J.; Farkas, N.; Ming, B.; Wagner, R.; Raman, A.; Moon, R. J.; Sabo, R.; Wegner, T. H., Development of the metrology and imaging of cellulose nanocrystals. *Measurement Science and Technology* **2010,** *22,* 024005.

49. Lindman, B.; Karlström, G.; Stigsson, L., On the mechanism of dissolution of cellulose. *Journal of Molecular Liquids* **2010,** *156,* 76.

50. Bochek, A., Effect of hydrogen bonding on cellulose solubility in aqueous and nonaqueous solvents. *Russian Journal of Applied Chemistry* **2003,** *76,* 1711.

51. Eriksen, Ø.; Syverud, K.; Gregersen, Ø., The use of microfibrillated cellulose produced from kraft pulp as strength enhancer in tmp paper. *Nordic Pulp & Paper Research Journal* **2008,** *23,* 299.

52. Saito, T.; Nishiyama, Y.; Putaux, J.-L.; Vignon, M.; Isogai, A., Homogeneous suspensions of individualized microfibrils from tempo-catalyzed oxidation of native cellulose. *Biomacromolecules* **2006,** *7,* 1687.

53. Pääkkö, M.; Ankerfors, M.; Kosonen, H.; Nykänen, A.; Ahola, S.; Österberg, M.; Ruokolainen, J.; Laine, J.; Larsson, P. T.; Ikkala, O., Enzymatic hydrolysis combined with mechanical shearing and high-pressure homogenization for nanoscale cellulose fibrils and strong gels. *Biomacromolecules* **2007,** *8,* 1934.

54. Pei, A.; Butchosa, N.; Berglund, L. A.; Zhou, Q., Surface quaternized cellulose nanofibrils with high water absorbency and adsorption capacity for anionic dyes. *Soft Matter* **2013,** *9,* 2047.

55. Liimatainen, H.; Visanko, M.; Sirviö, J.; Hormi, O.; Niinimäki, J., Sulfonated cellulose nanofibrils obtained from wood pulp through regioselective oxidative bisulfite pre-treatment. *Cellulose* **2013,** *20,* 741.

56. Huang, J.; Zhu, H.; Chen, Y.; Preston, C.; Rohrbach, K.; Cumings, J.; Hu, L., Highly transparent and flexible nanopaper transistors. *ACS Nano* **2013,** *7,* 2106.

57. Nogi, M.; Iwamoto, S.; Nakagaito, A. N.; Yano, H., Optically transparent nanofiber paper. *Advanced Materials* **2009,** *21,* 1595.

58. Siró, I.; Plackett, D., Microfibrillated cellulose and new nanocomposite materials: A review. *Cellulose* **2010,** *17,* 459.

59. Martoïa, F.; Perge, C.; Dumont, P.; Orgéas, L.; Fardin, M.; Manneville, S.; Belgacem, M., Heterogeneous flow kinematics of cellulose nanofibril suspensions under shear. *Soft Matter* **2015,** *11,* 4742.

60. Syverud, K.; Stenius, P., Strength and barrier properties of mfc films. *Cellulose* **2009,** *16,* 75.

61. Aulin, C.; Gällstedt, M.; Lindström, T., Oxygen and oil barrier properties of microfibrillated cellulose films and coatings. *Cellulose* **2010,** *17,* 559.

62. Lavoine, N.; Desloges, I.; Dufresne, A.; Bras, J., Microfibrillated cellulose–its barrier properties and applications in cellulosic materials: A review. *Carbohydrate Polymers* **2012,** *90,* 735.

63. Yang, Q.; Fukuzumi, H.; Saito, T.; Isogai, A.; Zhang, L., Transparent cellulose films with high gas barrier properties fabricated from aqueous alkali/urea solutions. *Biomacromolecules* **2011,** *12,* 2766.

64. Fukuzumi, H.; Saito, T.; Iwata, T.; Kumamoto, Y.; Isogai, A., Transparent and high gas barrier films of cellulose nanofibers prepared by tempo-mediated oxidation. *Biomacromolecules* **2008,** *10,* 162.

65. Benmalek, M.; Dunlop, H. M., Inorganic coatings on polymers. *Surface and Coatings Technology* **1995,** *76-77,* 821.

66. Chatham, H., Oxygen diffusion barrier properties of transparent oxide coatings on polymeric substrates. *Surface and Coatings Technology* **1996,** *78,* 1.

67. Jamieson, E.; Windle, A., Structure and oxygen-barrier properties of metallized polymer film. *Journal of Materials Science* **1983,** *18,* 64.

68. Graff, G. L.; Burrows, P. E.; Williford, R. E.; Praino, R. F., Barrier layer technology for flexible displays. *Flexible Flat Panel Displays* **2005,** 57.

69. Felts, J. T., Transparent barrier coatings update: Flexible substrates. *Journal of Plastic Film & Sheeting* **1993,** *9,* 139.

70. Park, J.-S.; Chae, H.; Chung, H. K.; Lee, S. I., Thin film encapsulation for flexible am-oled: A review. *Semiconductor Science and Technology* **2011,** *26,* 034001.

71. Tan, C.; Blackwood, D., Corrosion protection by multilayered conducting polymer coatings. *Corrosion Science* **2003,** *45,* 545.

72. Lewis, J., Material challenge for flexible organic devices. *Materials Today* **2006,** *9,* 38.

73. Nisato, G.; Kuilder, M.; Bouten, P.; Moro, L.; Philips, O.; Rutherford, N. In *P-88: Thin film encapsulation for oleds: Evaluation of multi-layer barriers using the ca test*, SID Symposium Digest of Technical Papers, Wiley Online Library: 2003; pp 550.

74. Zeng, Q.; Yu, A.; Lu, G.; Paul, D., Clay-based polymer nanocomposites: Research and commercial development. *Journal of nanoscience and nanotechnology* **2005,** *5,* 1574.

75. De Azeredo, H. M., Nanocomposites for food packaging applications. *Food Research International* **2009,** *42,* 1240.

76. Arora, A.; Padua, G., Nanocomposites in food packaging. *Journal of Food Science* **2010,** *75,* R43.

77. Tang, X.; Kumar, P.; Alavi, S.; Sandeep, K., Recent advances in biopolymers and biopolymer-based nanocomposites for food packaging materials. *Critical Reviews in Food Science and Nutrition* **2012,** *52,* 426.

78. Vaia, R. A.; Ishii, H.; Giannelis, E. P., Synthesis and properties of two-dimensional nanostructures by direct intercalation of polymer melts in layered silicates. *Chemistry of Materials* **1993,** *5,* 1694.

79. Liu, P., Polymer modified clay minerals: A review. *Applied Clay Science* **2007,** *38,* 64.

80. Decher, G., Fuzzy nanoassemblies: Toward layered polymeric multicomposites. *Science* **1997,** *277,* 1232.

81. Cho, C.; Culebras, M.; Wallace, K. L.; Song, Y.; Holder, K.; Hsu, J.-H.; Yu, C.; Grunlan, J. C., Stable n-type thermoelectric multilayer thin films with high power factor from carbonaceous nanofillers. *Nano Energy* **2016,** *28,* 426.

82. Xiang, Y.; Lu, S.; Jiang, S. P., Layer-by-layer self-assembly in the development of electrochemical energy conversion and storage devices from fuel cells to supercapacitors. *Chemical Society Reviews* **2012,** *41,* 7291.

83. Stierle, A., Tracking corrosion cracking. *Science* **2008,** *321,* 349.

84. Davis, J. R., *Corrosion of aluminum and aluminum alloys*. ASM International: 1999.

85. Association, A., *Aluminum: Properties and physical metallurgy*. ASM International: 1984.

86. Sørensen, P. A.; Kiil, S.; Dam-Johansen, K.; Weinell, C. E., Anticorrosive coatings: A review. *Journal of Coatings Technology and Research* **2009,** *6,* 135.

87. Gervasio, D.; Song, I.; Payer, J., Determination of the oxygen reduction products on astm a516 steel during cathodic protection. *Journal of Applied Electrochemistry* **1998,** *28,* 979.

88. Sørensen, P. A.; Kiil, S.; Dam-Johansen, K.; Weinell, C. E., Anticorrosive coatings: A review. *Journal of Coatings Technology and Research* **2009,** *6,* 135.

89. Twite, R.; Bierwagen, G., Review of alternatives to chromate for corrosion protection of aluminum aerospace alloys. *Progress in Organic Coatings* **1998,** *33,* 91.

90. Kulinich, S.; Akhtar, A., On conversion coating treatments to replace chromating for al alloys: Recent developments and possible future directions. *Russian Journal of Non-Ferrous Metals* **2012,** *53,* 176.

91. Vilche, J.; Bucharsky, E.; Giudice, C., Application of eis and sem to evaluate the influence of pigment shape and content in zrp formulations on the corrosion prevention of naval steel. *Corrosion Science* **2002,** *44,* 1287.

92. Kendig, M.; Buchheit, R., Corrosion inhibition of aluminum and aluminum alloys by soluble chromates, chromate coatings, and chromate-free coatings. *Corrosion* **2003,** *59,* 379.

93. Zhao, J.; Xia, L.; Sehgal, A.; Lu, D.; McCreery, R. L.; Frankel, G. S., Effects of chromate and chromate conversion coatings on corrosion of aluminum alloy 2024-t3. *Surface and Coatings Technology* **2001,** *140,* 51.

94. Xia, L.; Akiyama, E.; Frankel, G.; McCreery, R., Storage and release of soluble hexavalent chromium from chromate conversion coatings equilibrium aspects of cr vi concentration. *Journal of the Electrochemical Society* **2000,** *147,* 2556.

95. Wan, J.; Thompson, G.; Lu, K.; Smith, C., Chromium valence state in chromate conversion coatings on aluminium. *Physica B: Condensed Matter* **1995,** *208,* 511.

96. Williams, L. F. *Chromate conversion coatings on zinc*; DEFENCE STANDARDS LABS MARIBYRNONG (AUSTRALIA): 1972.

97. Gray, J.; Luan, B., Protective coatings on magnesium and its alloys—a critical review. *Journal of Alloys and Compounds* **2002,** *336,* 88.

98. Nordberg, G. F.; Fowler, B. A.; Nordberg, M., *Handbook on the toxicology of metals*. Academic Press: 2014.

99. Cook Jr, R.; Taylor, S., Pigment-derived inhibitors for aluminum alloy 2024-t3. *Corrosion* **2000,** *56,* 321.

100. Yong, Z.; Zhu, J.; Qiu, C.; Liu, Y., Molybdate/phosphate composite conversion coating on magnesium alloy surface for corrosion protection. *Applied Surface Science* **2008,** *255,* 1672.

101. Zheludkevich, M. L.; Shchukin, D. G.; Yasakau, K. A.; Möhwald, H.; Ferreira, M. G. J. C. o. M., Anticorrosion coatings with self-healing effect based on nanocontainers impregnated with corrosion inhibitor. *Chemistry of Materials* **2007,** *19,* 402.

102. Wei, H.; Wang, Y.; Guo, J.; Shen, N. Z.; Jiang, D.; Zhang, X.; Yan, X.; Zhu, J.; Wang, Q.; Shao, L., Advanced micro/nanocapsules for self-healing smart anticorrosion coatings. *Journal of Materials Chemistry A* **2015,** *3,* 469.

103. White, S. R.; Sottos, N.; Geubelle, P.; Moore, J.; Kessler, M. R.; Sriram, S.; Brown, E.; Viswanathan, S., Autonomic healing of polymer composites. *Nature* **2001,** *409,* 794.

104. Huang, M.; Yang, J., Salt spray and eis studies on hdi microcapsule-based self-healing anticorrosive coatings. *Progress in Organic Coatings* **2014,** *77,* 168.

105. Yuan, Y. C.; Rong, M. Z.; Zhang, M. Q.; Chen, J.; Yang, G. C.; Li, X. M., Self-healing polymeric materials using epoxy/mercaptan as the healant. *Macromolecules* **2008,** *41,* 5197.

106. Ghosh, S. K., *Self-healing materials: Fundamentals, design strategies, and applications*. John Wiley & Sons: 2009.

107. Kopeć, M.; Szczepanowicz, K.; Mordarski, G.; Podgórna, K.; Socha, R.; Nowak, P.; Warszyński, P.; Hack, T., Self-healing epoxy coatings loaded with inhibitor-containing polyelectrolyte nanocapsules. *Progress in Organic Coatings* **2015,** *84,* 97.

108. DeBerry, D. W., Modification of the electrochemical and corrosion behavior of stainless steels with an electroactive coating. *Journal of The Electrochemical Society* **1985,** *132,* 1022.

109. Tallman, D.; Pae, Y.; Bierwagen, G., Conducting polymers and corrosion: Part 2—polyaniline on aluminum alloys. *Corrosion* **2000,** *56,* 401.

110. Tallman, D. E.; Spinks, G.; Dominis, A.; Wallace, G. G., Electroactive conducting polymers for corrosion control. *Journal of Solid State Electrochemistry* **2002,** *6,* 73.

111. Riaz, U.; Nwaoha, C.; Ashraf, S., Recent advances in corrosion protective composite coatings based on conducting polymers and natural resource derived polymers. *Progress in Organic Coatings* **2014,** *77,* 743.

112. Deshpande, P. P.; Jadhav, N. G.; Gelling, V. J.; Sazou, D., Conducting polymers for corrosion protection: A review. *Journal of Coatings Technology and Research* **2014,** *11,* 473.

113. Yang, C.; Wei, H.; Guan, L.; Guo, J.; Wang, Y.; Yan, X.; Zhang, X.; Wei, S.; Guo, Z., Polymer nanocomposites for energy storage, energy saving, and anticorrosion. *Journal of Materials Chemistry A* **2015,** *3,* 14929.

114. González-García, Y.; González, S.; Souto, R., Electrochemical and structural properties of a polyurethane coating on steel substrates for corrosion protection. *Corrosion Science* **2007,** *49,* 3514.

115. Chattopadhyay, D. K.; Raju, K., Structural engineering of polyurethane coatings for high performance applications. *Progress in Polymer Science* **2007,** *32,* 352.

116. Noble, K.-L., Waterborne polyurethanes. *Progress in Organic Coatings* **1997,** *32,* 131.

117. Christopher, G.; Kulandainathan, M. A.; Harichandran, G., Biopolymers nanocomposite for material protection: Enhancement of corrosion protection using waterborne polyurethane nanocomposite coatings. *Progress in Organic Coatings* **2016,** *99,* 91.

118. Christopher, G.; Kulandainathan, M. A.; Harichandran, G., Highly dispersive waterborne polyurethane/zno nanocomposites for corrosion protection. *Journal of Coatings Technology and Research* **2015,** *12,* 657.

119. Yeh, J.-M.; Yao, C.-T.; Hsieh, C.-F.; Lin, L.-H.; Chen, P.-L.; Wu, J.-C.; Yang, H.-C.; Wu, C.-P., Preparation, characterization and electrochemical corrosion studies on

environmentally friendly waterborne polyurethane/na+-mmt clay nanocomposite coatings. *European Polymer Journal* **2008,** *44,* 3046.

120. Christopher, G.; Kulandainathan, M. A.; Harichandran, G., Comparative study of effect of corrosion on mild steel with waterborne polyurethane dispersion containing graphene oxide versus carbon black nanocomposites. *Progress in Organic Coatings* **2015,** *89,* 199.

121. Song, Y.; Hagen, D. A.; Qin, S.; Holder, K. M.; Falke, K.; Grunlan, J. C., Edge charge neutralization of clay for improved oxygen gas barrier in multilayer nanobrick wall thin films. *ACS Applied Materials & Interfaces* **2016**.

122. Soltani, I.; Smith, S. D.; Spontak, R. J., Effect of polyelectrolyte on the barrier efficacy of layer-by-layer nanoclay coatings. *Journal of Membrane Science* **2016**.

123. Song, Y.; Tzeng, P.; Grunlan, J. C., Super oxygen and improved water vapor barrier of polypropylene film with polyelectrolyte multilayer nanocoatings. *Macromolecular Rapid Communications* **2016,** *37,* 963.

124. Holder, K. M.; Spears, B. R.; Huff, M. E.; Priolo, M. A.; Harth, E.; Grunlan, J. C., Stretchable gas barrier achieved with partially hydrogen-bonded multilayer nanocoating. *Macromolecular Rapid Communications* **2014,** *35,* 960.

125. Xiang, F.; Ward, S. M.; Givens, T. M.; Grunlan, J. C., Super stretchy polymer multilayer thin film with high gas barrier. *ACS Macro Letters* **2014,** *3,* 1055.

126. Kharlampieva, E.; Sukhishvili, S. A., Hydrogen-bonded layer-by-layer polymer films. *Journal of Macromolecular Science, Part C: Polymer Reviews* **2006,** *46,* 377.

127. Lutkenhaus, J. L.; Hrabak, K. D.; McEnnis, K.; Hammond, P. T., Elastomeric flexible free-standing hydrogen-bonded nanoscale assemblies. *Journal of the American Chemical Society* **2005,** *127,* 17228.

128. Xiang, F.; Givens, T. M.; Ward, S. M.; Grunlan, J. C., Elastomeric polymer multilayer thin film with sustainable gas barrier at high strain. *ACS Applied Materials & Interfaces* **2015,** *7,* 16148.

129. Humood, M.; Chowdhury, S.; Song, Y.; Tzeng, P.; Grunlan, J. C.; Polycarpou, A. A., Nanomechanical behavior of high gas barrier multilayer thin films. *ACS Applied Materials & Interfaces* **2016,** *8,* 11128.

130. Gamboa, D.; Priolo, M. A.; Ham, A.; Grunlan, J. C., Note: Influence of rinsing and drying routines on growth of multilayer thin films using automated deposition system. *Review of Scientific Instruments* **2010,** *81,* 036103.

131. Jang, W.-S.; Grunlan, J. C., Robotic dipping system for layer-by-layer assembly of multifunctional thin films. *Review of Scientific Instruments* **2005,** *76,* 103904.

132. Picart, C.; Mutterer, J.; Richert, L.; Luo, Y.; Prestwich, G. D.; Schaaf, P.; Voegel, J.-C.; Lavalle, P., Molecular basis for the explanation of the exponential growth of polyelectrolyte multilayers. *Proceedings of the National Academy of Sciences* **2002,** *99,* 12531.

133. Lavalle, P.; Gergely, C.; Cuisinier, F.; Decher, G.; Schaaf, P.; Voegel, J.; Picart, C., Comparison of the structure of polyelectrolyte multilayer films exhibiting a linear and an exponential growth regime: An in situ atomic force microscopy study. *Macromolecules* **2002,** *35,* 4458.

134. Salehi, A.; Desai, P. S.; Li, J.; Steele, C. A.; Larson, R. G., Relationship between polyelectrolyte bulk complexation and kinetics of their layer-by-layer assembly. *Macromolecules* **2015,** *48,* 400.

135. Tombácz, E.; Szekeres, M., Colloidal behavior of aqueous montmorillonite suspensions: The specific role of ph in the presence of indifferent electrolytes. *Applied Clay Science* **2004,** *27,* 75.

136. Fareed, M. A.; Stamboulis, A., Nanoclays reinforced glass ionomer cements: Dispersion and interaction of polymer grade (pg) montmorillonite with poly (acrylic acid). *Journal of Materials Science: Materials in Medicine* **2014,** *25,* 91.

137. Shi, Y.; Xue, Z.; Wang, X.; Wang, L.; Wang, A., Removal of methylene blue from aqueous solution by sorption on lignocellulose-g-poly (acrylic acid)/montmorillonite three-dimensional cross-linked polymeric network hydrogels. *Polymer Bulletin* **2013,** *70,* 1163.

138. Tran, N. H.; Dennis, G. R.; Milev, A. S.; Kannangara, G. K.; Wilson, M. A.; Lamb, R. N., Interactions of sodium montmorillonite with poly (acrylic acid). *Journal of Colloid and Interface Science* **2005,** *290,* 392.

139. Haraguchi, K.; Takehisa, T., Nanocomposite hydrogels: A unique organic-inorganic network structure with extraordinary mechanical, optical, and swelling/de-swelling properties. *Advanced Materials* **2002,** *14,* 1120.

140. Qiu, H.; Yu, J., Polyacrylate/(carboxymethylcellulose modified montmorillonite) superabsorbent nanocomposite: Preparation and water absorbency. *Journal of Applied Polymer Science* **2008,** *107,* 118.

141. Tran, N.; Wilson, M.; Milev, A.; Dennis, G.; Kannangara, G.; Lamb, R., Dispersion of silicate nano-plates within poly (acrylic acid) and their interfacial interactions. *Science and Technology of Advanced Materials* **2006,** *7,* 786.

142. Priolo, M. A.; Gamboa, D.; Grunlan, J. C., Transparent clay−polymer nano brick wall assemblies with tailorable oxygen barrier. *ACS Applied Materials & Interfaces* **2010,** *2,* 312.

143. Cho, C.; Xiang, F.; Wallace, K. L.; Grunlan, J. C., Combined ionic and hydrogen bonding in polymer multilayer thin film for high gas barrier and stretchiness. *Macromolecules* **2015,** *48,* 5723.

144. Erbaş, A.; Horinek, D.; Netz, R. R., Viscous friction of hydrogen-bonded matter. *Journal of the American Chemical Society* **2011,** *134,* 623.

145. Roberts, A.; Henry, B.; Sutton, A.; Grovenor, C.; Briggs, G.; Miyamoto, T.; Kano, M.; Tsukahara, Y.; Yanaka, M., Gas permeation in silicon-oxide/polymer (sio x/pet) barrier films: Role of the oxide lattice, nano-defects and macro-defects. *Journal of Membrane Science* **2002,** *208,* 75.

146. Wågberg, L.; Decher, G.; Norgren, M.; Lindström, T.; Ankerfors, M.; Axnäs, K., The build-up of polyelectrolyte multilayers of microfibrillated cellulose and cationic polyelectrolytes. *Langmuir* **2008,** *24,* 784.

147. Turbak, A. F.; Snyder, F. W.; Sandberg, K. R. In *Microfibrillated cellulose, a new cellulose product: Properties, uses, and commercial potential*, J. Appl. Polym. Sci.: Appl. Polym. Symp.;United States, ITT Rayonier Inc., Shelton, WA: Jan., 1983.

148. Khalil, H. A.; Bhat, A.; Yusra, A. I., Green composites from sustainable cellulose nanofibrils: A review. *Carbohydrate Polymers* **2012,** *87,* 963.

149. Herrick, F. W.; Casebier, R. L.; Hamilton, J. K.; Sandberg, K. R. In *Microfibrillated cellulose: Morphology and accessibility*, J. Appl. Polym. Sci.: Appl. Polym. Symp.;(United States), ITT Rayonier Inc., Shelton, WA: 1983.

150. Sorrentino, A.; Gorrasi, G.; Vittoria, V., Potential perspectives of bio-nanocomposites for food packaging applications. *Trends in Food Science & Technology* **2007,** *18,* 84.

151. Lewin, M.; Basch, A., Structure, pyrolysis, and flammability of cellulose. In *Flame-retardant polymeric materials*, Springer: 1978; pp 1.

152. Liu, A.; Walther, A.; Ikkala, O.; Belova, L.; Berglund, L. A., Clay nanopaper with tough cellulose nanofiber matrix for fire retardancy and gas barrier functions. *Biomacromolecules* **2011,** *12,* 633.

153. Jin, H.; Cao, A.; Shi, E.; Seitsonen, J.; Zhang, L.; Ras, R. H.; Berglund, L. A.; Ankerfors, M.; Walther, A.; Ikkala, O., Ionically interacting nanoclay and nanofibrillated cellulose lead to tough bulk nanocomposites in compression by forced self-assembly. *Journal of Materials Chemistry B* **2013,** *1,* 835.

154. Wang, Q.; Guo, J.; Xu, D.; Cai, J.; Qiu, Y.; Ren, J.; Zhang, L., Facile construction of cellulose/montmorillonite nanocomposite biobased plastics with flame retardant and gas barrier properties. *Cellulose* **2015,** *22,* 3799.

155. Wu, C.-N.; Saito, T.; Fujisawa, S.; Fukuzumi, H.; Isogai, A., Ultrastrong and high gas-barrier nanocellulose/clay-layered composites. *Biomacromolecules* **2012,** *13,* 1927.

156. Liu, A.; Berglund, L. A., Clay nanopaper composites of nacre-like structure based on montmorrilonite and cellulose nanofibers—improvements due to chitosan addition. *Carbohydrate Polymers* **2012,** *87,* 53.

157. Wang, J.; Cheng, Q.; Lin, L.; Jiang, L., Synergistic toughening of bioinspired poly (vinyl alcohol)–clay–nanofibrillar cellulose artificial nacre. *ACS Nano* **2014,** *8,* 2739.

158. Hasani, M.; Cranston, E. D.; Westman, G.; Gray, D. G., Cationic surface functionalization of cellulose nanocrystals. *Soft Matter* **2008,** *4,* 2238.

159. Nordenström, M.; Fall, A.; Nyström, G.; Wågberg, L., Formation of colloidal nanocellulose glasses and gels. *Langmuir* **2017,** *33,* 9772.

160. Yao, K.; Huang, S.; Tang, H.; Xu, Y.; Buntkowsky, G.; Berglund, L. A.; Zhou, Q., Bioinspired interface engineering for moisture resistance in nacre-mimetic cellulose nanofibrils/clay nanocomposites. *ACS Applied Materials & Interfaces* **2017**.

161. Laufer, G.; Kirkland, C.; Cain, A. A.; Grunlan, J. C., Clay–chitosan nanobrick walls: Completely renewable gas barrier and flame-retardant nanocoatings. *ACS Applied Materials & Interfaces* **2012,** *4,* 1643.

162. Chapple, S.; Anandjiwala, R., Flammability of natural fiber-reinforced composites and strategies for fire retardancy: A review. *Journal of Thermoplastic Composite Materials* **2010,** *23,* 871.

163. Smith, R. J.; Holder, K. M.; Ruiz, S.; Hahn, W.; Song, Y.; Lvov, Y. M.; Grunlan, J. C., Environmentally benign halloysite nanotube multilayer assembly significantly reduces polyurethane flammability. *Advanced Functional Materials* **2017,** 1703289.

164. Yao, K.; Huang, S.; Tang, H.; Xu, Y.; Buntkowsky, G.; Berglund, L. A.; Zhou, Q., Bioinspired interface engineering for moisture resistance in nacre-mimetic cellulose nanofibrils/clay nanocomposites. *ACS Applied Materials & Interfaces* **2017,** *9,* 20169.

165. Podsiadlo, P.; Shim, B. S.; Kotov, N. A., Polymer/clay and polymer/carbon nanotube hybrid organic–inorganic multilayered composites made by sequential layering of nanometer scale films. *Coordination Chemistry Reviews* **2009,** *253,* 2835.

166. Roberts, A.; Henry, B.; Sutton, A.; Grovenor, C.; Briggs, G.; Miyamoto, T.; Kano, M.; Tsukahara, Y.; Yanaka, M., Gas permeation in silicon-oxide/polymer (siox/pet) barrier films: Role of the oxide lattice, nano-defects and macro-defects. *Journal of Membrane Science* **2002,** *208,* 75.

167. Li, J.; Wu, R.; Jing, Z.; Yan, L.; Zha, F.; Lei, Z., One-step spray-coating process for the fabrication of colorful superhydrophobic coatings with excellent corrosion resistance. *Langmuir* **2015,** *31,* 10702.

168. Yan, M.; Vetter, C. A.; Gelling, V. J., Corrosion inhibition performance of polypyrrole al flake composite coatings for al alloys. *Corrosion Science* **2013,** *70,* 37.

169. Carneiro, J.; Tedim, J.; Ferreira, M., Chitosan as a smart coating for corrosion protection of aluminum alloy 2024: A review. *Progress in Organic Coatings* **2015,** *89,* 348.

170. Leggat, R.; Taylor, S.; Zhang, W.; Buchheit, R., Corrosion performance of field-applied chromate conversion coatings. *Corrosion* **2002,** *58,* 283.

171. Andreeva, D. V.; Fix, D.; Mohwald, H.; Shchukin, D. G., Self-healing anticorrosion coatings based on ph-sensitive polyelectrolyte/inhibitor sandwichlike nanostructures. *Advanced Materials* **2008,** *20,* 2789.

172. Andreeva, D. V.; Fix, D.; Möhwald, H.; Shchukin, D. G., Buffering polyelectrolyte multilayers for active corrosion protection. *Journal of Materials Chemistry* **2008,** *18,* 1738.

173. Priolo, M. A.; Holder, K. M.; Greenlee, S. M.; Grunlan, J. C., Transparency, gas barrier, and moisture resistance of large-aspect-ratio vermiculite nanobrick wall thin films. *ACS Applied Materials & Interfaces* **2012,** *4,* 5529.

174. Priolo, M. A.; Holder, K. M.; Greenlee, S. M.; Stevens, B. E.; Grunlan, J. C., Precisely tuning the clay spacing in nanobrick wall gas barrier thin films. *Chemistry of Materials* **2013,** *25,* 1649.

175. Farhat, T. R.; Schlenoff, J. B., Doping-controlled ion diffusion in polyelectrolyte multilayers: Mass transport in reluctant exchangers. *Journal of the American Chemical Society* **2003,** *125,* 4627.

176. Schlenoff, J. B., Charge balance and transport in ion-paired polyelectrolyte multilayers. *Multilayer Thin Films: Sequential Assembly of Nanocomposite Materials, Second Edition* **2012,** 281.

177. Cubides, Y.; Castaneda, H., Corrosion protection mechanisms of carbon nanotube and zinc-rich epoxy primers on carbon steel in simulated concrete pore solutions in the presence of chloride ions. *Corrosion Science* **2016,** *109,* 145.

178. Eslami, M.; Fedel, M.; Speranza, G.; Deflorian, F.; Zanella, C., Deposition and characterization of cerium-based conversion coating on hpdc low si content aluminum alloy. *Journal of The Electrochemical Society* **2017,** *164,* C581.

179. Su, C.; Wu, W.; Li, Z.; Guo, Y., Prediction of film performance by electrochemical impedance spectroscopy. *Corrosion Science* **2015,** *99,* 42.

180. Trdan, U.; Grum, J., Sem/eds characterization of laser shock peening effect on localized corrosion of al alloy in a near natural chloride environment. *Corrosion Science* **2014,** *82,* 328.

181. Mansfeld, F.; Tsai, C., Determination of coating deterioration with eis: I. Basic relationships. *Corrosion* **1991,** *47,* 958.

182. Harb, S. V.; Pulcinelli, S. H.; Santilli, C. V.; Knowles, K. M.; Hammer, P., A comparative study on graphene oxide and carbon nanotube reinforcement of pmma-siloxane-silica anticorrosive coatings. *ACS applied materials & interfaces* **2016,** *8,* 16339.

183. Scully, J. R., Polarization resistance method for determination of instantaneous corrosion rates. *Corrosion* **2000,** *56,* 199.

184. Fan, F.; Zhou, C.; Wang, X.; Szpunar, J., Layer-by-layer assembly of a self-healing anticorrosion coating on magnesium alloys. *Acs Applied Materials & Interfaces* **2015,** *7,* 27271.

185. Andreeva, D. V.; Fix, D.; Möhwald, H.; Shchukin, D. G., Self-healing anticorrosion coatings based on ph-sensitive polyelectrolyte/inhibitor sandwichlike nanostructures. *Advanced Materials* **2008,** *20,* 2789.

186. Wang, D.; Bierwagen, G. P., Sol–gel coatings on metals for corrosion protection. *Progress in Organic Coatings* **2009,** *64,* 327.

187. Sanchez-Garcia, M. D.; Lopez-Rubio, A.; Lagaron, J. M., Natural micro and nanobiocomposites with enhanced barrier properties and novel functionalities for food biopackaging applications. *Trends in Food Science & Technology* **2010,** *21,* 528.

188. Jung, K.; Bae, J.-Y.; Park, S. J.; Yoo, S.; Bae, B.-S., High performance organic-inorganic hybrid barrier coating for encapsulation of oleds. *Journal of Materials Chemistry* **2011,** *21,* 1977.

189. Wang, L.; Ruan, C.; Li, M.; Zou, J.; Tao, H.; Peng, J.; Xu, M., Enhanced moisture barrier performance for ald-encapsulated oleds by introducing an organic protective layer. *Journal of Materials Chemistry C* **2017,** *5,* 4017.

190. Song, Y.; Meyers, K. P.; Gerringer, J.; Ramakrishnan, R. K.; Humood, M.; Qin, S.; Polycarpou, A. A.; Nazarenko, S.; Grunlan, J. C., Fast self-healing of polyelectrolyte multilayer nanocoating and restoration of super oxygen barrier. *Macromolecular Rapid Communications* **2017,** *38,* 1700064.

191. Vogt, B. D.; Soles, C. L.; Lee, H.-J.; Lin, E. K.; Wu, W.-l., Moisture absorption and absorption kinetics in polyelectrolyte films: Influence of film thickness. *Langmuir* **2004,** *20,* 1453.

192. Granberg, H.; Gustafsson Coppel, L.; Eita, M.; de Mayolo, E. A.; Arwin, H.; Wågberg, L., Dynamics of moisture interaction with polyelectrolyte multilayers containing nanofibrillated cellulose. *Nordic Pulp & Paper Research Journal* **2012,** *27,* 496.

193. Licari, J. J.; Swanson, D. W., *Adhesives technology for electronic applications: Materials, processing, reliability*. William Andrew: 2011.

194. Logothetidis, S., *Handbook of flexible organic electronics: Materials, manufacturing and applications*. Elsevier: 2014.

195. Czeremuszkin, G.; Latreche, M.; Wertheimer, M.; da Silva Sobrinho, A., Ultrathin silicon-compound barrier coatings for polymeric packaging materials: An industrial perspective. *Plasmas and Polymers* **2001,** *6,* 107.

196. Chappell, C.; Mason, E. L.; Siddiqui, J. A., Amine functional specialty polymers as adhesives in multilayer film composite structures. In *Specialty monomers and polymers*, American Chemical Society: 2000; Vol. 755, pp 186.

197. Kim, M. T., Influence of substrates on the elastic reaction of films for the microindentation tests. *Thin Solid Films* **1996,** *283,* 12.

198. Chen, Y.; Ye, Y.; Chen, Z.-R., Vapor-based synthesis of bilayer anti-corrosion polymer coatings with excellent barrier property and superhydrophobicity. *Journal of Materials Science* **2019,** *54,* 5907.

199. Zhu, G. H.; Cho, S.-H.; Zhang, H.; Zhao, M.; Zacharia, N. S., Slippery liquid-infused porous surfaces (slips) using layer-by-layer polyelectrolyte assembly in organic solvent. *Langmuir* **2018,** *34,* 4722.

200. Wong, T.-S.; Kang, S. H.; Tang, S. K.; Smythe, E. J.; Hatton, B. D.; Grinthal, A.; Aizenberg, J., Bioinspired self-repairing slippery surfaces with pressure-stable omniphobicity. *Nature* **2011,** *477,* 443.

201. Sunny, S.; Vogel, N.; Howell, C.; Vu, T. L.; Aizenberg, J., Lubricant-infused nanoparticulate coatings assembled by layer-by-layer deposition. *Advanced Functional Materials* **2014,** *24,* 6658.

202. Kim, P.; Wong, T.-S.; Alvarenga, J.; Kreder, M. J.; Adorno-Martinez, W. E.; Aizenberg, J., Liquid-infused nanostructured surfaces with extreme anti-ice and anti-frost performance. *ACS Nano* **2012,** *6,* 6569.

203. Howell, C.; Vu, T. L.; Lin, J. J.; Kolle, S.; Juthani, N.; Watson, E.; Weaver, J. C.; Alvarenga, J.; Aizenberg, J., Self-replenishing vascularized fouling-release surfaces. *ACS Applied Materials & Interfaces* **2014,** *6,* 13299.